Microstructural and metabolic alterations in the zebrafish brain induced by toll-like receptor 2 deficiency: insights from ultra-high field magnetic resonance imaging and spectroscopy

Singer, R.

3

ULTRA-HIGH FIELD DIFFUSION MRI UNCOVERS INTRIGUING MICROSTRUCTURAL CHANGES IN THE ADULT ZEBRAFISH BRAIN CAUSED BY TLR2 GENOMIC DELETION*

* This chapter was published in NMR BIOMED 2024; doi:10.1002/nbm.5170

ABSTRACT

The toll-like receptor 2 (TLR2) belongs to the TLR protein family that plays an important role in the immune and inflammation response system. While TLR2 is predominantly expressed in immune cells, its expression has also been detected in the brain, specifically in microglia and astrocytes. Recent studies indicate that genomic deletion of TLR2 can result in impaired neurobehavioral function. It is currently not clear if the genomic deletion of TLR2 leads to any alterations in the microstructural features of the brain. In the current study, we non-invasively assess microstructural changes in the brain of TLR2 deficient (*tlr2*$^{-/-}$) zebrafish using state-of-the art MRI methods at ultra-high magnetic field strength (17.6 T). A significant increase in cortical thickness and an overall trend towards increased brain volumes were observed in young *tlr2*$^{-/-}$ zebrafish. An elevated T_2 relaxation time and significantly reduced apparent diffusion coefficient (*ADC*) unveil brain wide microstructural alterations, potentially indicative of cytotoxic edema and astrogliosis in the *tlr2*$^{-/-}$ zebrafish. Multi-component analysis of the *ADC* diffusivity signal by the phasor approach shows an increase in the slow *ADC* component associated with restricted diffusion. Diffusion tensor imaging and diffusion kurtosis imaging analysis revealed diminished diffusivity and enhanced kurtosis in various white matter tracks in *tlr2*$^{-/-}$ as compared to control zebrafish, identifying the microstructural underpinnings associated with compromised white matter integrity and axonal degeneration. Taken together, our findings demonstrate that the genomic deletion of TLR2 results in severe alterations to the microstructural features of the zebrafish brain. This study also highlights the potential of ultra-high field diffusion MRI techniques in discerning exceptionally fine microstructural details within the small zebrafish brain, offering potential for investigating microstructural changes in zebrafish models of various brain diseases.

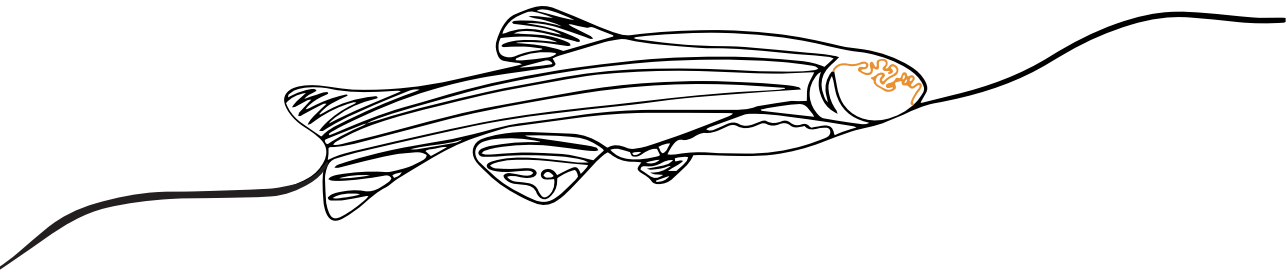

1. INTRODUCTION

Pattern recognition receptors (PRRs), encoded in the germline DNA, play a crucial role in the animal immune defence as part of the innate immune system[1]. Unlike T cells and B cells, expressing antigen recognition receptors with a high specificity, PRRs initiate immune response by recognizing a diverse array of pathogen-associated molecular patterns (PAMPs), found on various microorganisms. PRRs also recognise danger-associated molecular patterns (DAMPs), produced as a consequence of damaged tissue. Among the eight PRR groups[2], Toll-like receptors (TLRs) stand out as vital components of the innate immune system. Structurally, TLRs consist of three distinct parts[3]; (1) an N-terminal ectodomain on the membrane outside, responsible for recognizing and binding to specific PAMPs or DAMPs, (2) a transmembrane domain spanning the lipid bilayer of the cell membrane, to anchor the receptor in its place, and (3) a C-terminal to initiate downstream signalling on the intracellular side of the membrane. Within the TLR family, specific TLRs play crucial roles in distinguishing unique PAMPs and DAMPs. Interestingly, the number of TLRs expressed in various vertebrate species varies. For example, humans possess 10 TLRs encoded in their genome, whereas mice and zebrafish have genomes encoding for at least 12, and 20 functional TLRs, respectively[4,5]. Toll-like receptor 2 (TLR2), one such member of the TLR family, plays a particularly important role in the immune- and inflammation response system and has orthologs in humans, mice, and zebrafish. TLR2 is expressed on the cell surface of endothelial, epithelial, and immune cells, including macrophages, dendritic cells and monocytes[6], and forms heterodimers with TLR1 or TLR6[2]. The broad recognition spectrum of TLR2 encompasses a wide range of PAMPs and DAMPs ligands[2]. In addition to its crucial role in the immune and inflammatory response system, TLR2 has become a focal point of interest due to its dual function in the infection processes. While TLR2-mediated inflammatory responses are important for effective bacterial clearance, excessive or inappropriate TLR2 signalling can lead to unintended tissue damage, inflammatory disorders, or delayed healing[7,8]. In the brain, excessive TLR2 signalling has emerged as potential player in the pathogenesis of neuroinflammatory and neurodegenerative disorders, including in the pathogenesis of Alzheimer's disease, Parkinson's disease, amyotrophic lateral sclerosis, and ischemic strokes[9]. There are rather conflicting reports on the role of TLR2 deficiency in the brain. Some reports suggest that a deficiency of TLR2 may improve neurobehavioral functions and protect against neurodegenerative diseases[10]. On the other hand, other reports have shown that a deficiency of TLR2 itself could induce cognitive disabilities, decreased locomotor activity, and increased anxiety and depression[11,12]. In a TLR2-deficient mouse model, aggravated white matter damage and deteriorated neurobehavioral functions have been observed in the absence of an infection or neurodegenerative inducing mutations[11]. Thus, the exact role of TLR2 in regulating normal neurological functions and inducing neuroinflammatory processes remains to be established.

In a recent study, we utilized zebrafish (*Danio rerio*) larvae as an *in vivo* model to investigate the metabolic control functions of TLR2 through transcriptomic and metabolomic approaches[2]. We showed that the deficiency of TLR2 in zebrafish larvae leads to many metabolic changes compared to controls and proposed that in addition to its function in immunity and inflammatory processes, TLR2 has a function in controlling metabolism in the absence of infection. However, the impact of TLR deficiency on brain structure and function and neuroinflammation in the absence of infection is not clear. A comprehensive, non-invasive system-level study would be necessary to clarify this. Magnetic resonance imaging (MRI) is a well-established, non-invasive technique. MRI provides distinct advantages compared to other microscopic techniques, even those potentially reaching higher resolutions. This includes its capability for whole-organ imaging, including full three-dimensional analysis, while eliminating the necessity for sectioning or chemical staining. Moreover, recent advancements in MRI gradient systems and ultra-high magnetic field strength provide the ability to achieve very high spatial resolutions[13]. In our earlier studies we developed MRI methods for (*in vivo)* imaging of zebrafish[14,15], which we applied to study various models including cystic leukoencephalopathy[16], Lowe syndrome[17], *in vivo* analysis of tumors[18] and microstructural changes in the muscle tissue of leptin-deficient zebrafish[19]. *In vivo* MRI also allowed longitudinal studies of live adult zebrafish brain as reported by Hamilton *et al.* [20]. However, getting access to microstructural details in the tiny zebrafish brain is challenging. MRI at ultra-high field in conjunction with mathematical modelling can probe microstructural changes in tiny zebrafish brain. In addition, diffusion-based MRI (dMRI) offer a remarkable sensitivity to water movement, encompassing techniques including diffusion-weighted imaging (DWI), diffusion tensor imaging (DTI), and diffusion kurtosis imaging (DKI). These techniques provide unique ways for exploring microstructural alterations in the brain and offer non-invasive opportunities to monitor the progression of neurodegenerative disorders[21,22]. Furthermore, dMRI tractography enables the visualization of white matter structures within the zebrafish brain, thereby enabling the precise examination of these anatomical structures[23].

To elucidate the precise involvement of TLR2 in regulating normal neurological functions and neuroinflammatory processes, we employed TLR2 knockout (*tlr2*$^{-/-}$) zebrafish as a model organism. By utilizing state-of-the-art MRI methods at ultra-high magnetic field (17.6 T) we explored the impact of TLR2 deficiency on the microarchitecture of the brain. Ultra-high field micro-MRI with strong field gradients provides the necessary resolution and signal-to-noise required to study the micro-structural changes in the tiny zebrafish brain. Furthermore, diffusion-weighted MRI provided superior anatomical and substructural details of the zebrafish brain as compared to traditional anatomical imaging. DTI tractography by short-track track-density imaging enabled us to see changes in specific white matter structures in *tlr2*$^{-/-}$ zebrafish as compared to controls. Our results show that TLR2 deficiency leads to

microstructural changes associated with compromised white matter integrity and axonal degeneration.

2. METHODS

Zebrafish husbandry

In this study, the wild type AB/TL strain and *tlr2*^{sa19423} zebrafish line, obtained from the Sanger Institute Zebrafish Mutation Resource (Hinxton, Cambridge, UK) were utilized. The homozygote carriers of the TLR2 mutation, along with their wild type control, were subjected to over five rounds of outcrossing, resulting in the *tlr2*$^{-/-}$ (mutant) and *tlr2*$^{+/+}$ (control) siblings used for the experiments described in this work. Screening and raising of *tlr2*$^{-/-}$ and control zebrafish were performed as previously described[24,25], complying with university animal welfare committee guidelines (Licence numbers AVD1060020171767 and AVD10600202216175), following EU Animal Protection Directive international guidelines (2010/63/EU), and according to standard protocols (www.zfin.org). For imaging, five male pairs of three-month-old (84 days) *tlr2*$^{-/-}$ and control zebrafish, were euthanized through immobilization by submersion in ice water (0 – 4 °C) for approximately 10 minutes, followed by cessation of opercular movement. Specimen were then fixed in 4% buffered paraformaldehyde (Zinc Formal-Fixx, ThermoShandon, UK) for 4 days.

Magnetic Resonance Imaging

MR imaging experiments were conducted with a Bruker vertical bore system (Bruker Biospin GmbH, Germany) operating at 17.6 T (750 MHz). The system was equipped with a water-cooled Micro5 gradient system, offering a gradient strength (G_{max}) up to 3 T/m. Additionally, a birdcage transmit and receive radiofrequency (RF) coil with a 5 mm inner diameter and a GREAT60 gradient power supply were employed. Data acquisition and processing was performed with a Linux workstation, running ParaVision 360 v3.3 imaging software (Bruker BioSpin GmbH, Germany). For all experiments, zebrafish were transferred to 5 mm NMR tubes and embedded in perfluoropolyether (Fomblin Y, Solvay Solexis S.P.A.) to remove background signals whilst having a susceptibility close to tissue[26]. Maximum signal intensity and magnetic field homogeneity were achieved by aligning the zebrafish brain to the centre of the RF coil and automatic second-order shimming. Prior to each experiment, the frequency calibration was fine-tuned, and the reference power and receiver gain were optimized.

For the estimation of T_2, we utilized a multi-slice multi-echo (MSME) pulse sequence, based on the Carr-Purcell Meiboom-Gill (CPMG) sequence[27]. MSME measurements were performed with 60 echoes per excitation, with a CPMG refocusing pulse interval τ = 6.0 ms, a repetition time TR = 3000 ms, and ns = 4 for averaging. The field of view (FOV) was 6 × 6 mm, with a

matrix size of 128 × 128, resulting in an in-plane resolution of 47 × 47 µm, at a slice thickness of 500 µm and a total scan time of ~ 25 minutes.

In a diffusion-based MRI (dMRI) experiment, a 90° excitation RF pulse is succeeded by a 180° refocusing RF pulse. Manifestation of diffusion dependency is achieved through application of gradient pulses both before and after the refocusing RF pulse, as originally developed by Stejskal and Tanner[28]. The strength (G), gradient pulse interval (Δ) and gradient pulse length (δ) of these gradient pulses are summarised in the b-value according to $b = \gamma^2 \cdot G^2 \cdot \delta^2 \cdot \left(\Delta - \frac{\delta}{3}\right)$, where γ is the gyromagnetic ratio. DWI experiments were performed with a diffusion-weighted spin echo sequence, applying an echo time TE = 13.0 ms, TR = 1000 ms, ns = 4, δ = 1 ms, Δ = 7 ms, and an effective b-value range of 50, 500, 1000, 1500, 2000, 2500, or 3000 s/mm^2. The FOV was 6 × 6 mm, with a matrix size of 128 × 128, resulting in an in-plane resolution of 47 × 47 µm, at a slice thickness of 200 µm and a total scan time of ~ 48 minutes. DTI utilizing echo-planar imaging (EPI) was employed for anatomical imaging of the zebrafish brain. Additionally, this technique enabled the estimation of various diffusion metrics including axial diffusivity ($D_\parallel$), radial diffusivity ($D_\perp$), mean diffusivity (MD), fractional anisotropy (FA), as well as axial kurtosis ($K_\parallel$), radial kurtosis ($K_\perp$) mean kurtosis tensor (MK), and kurtosis fractional anisotropy (KFA). In addition, DTI facilitated tractography was used to explore the connectivity of neural pathways within the zebrafish brain. 2D DTI experiments were performed with TE = 12.4 ms, TR = 2000 ms, ns = 32, and an EPI factor of 8. Multi-shell DTI experiments were performed with δ = 1.5 ms, Δ = 6 ms, and an effective b-value range of 4, 1000, 3500, or 6000 s/mm^2, with 8, 12, 24, or 36 diffusion-encoding directions, respectively. The FOV was 5 × 5 mm, with a matrix size of 200 × 200, resulting in an in-plane resolution of 25 × 25 µm, at a slice thickness of 200 µm and a total scan time of 11 hours, 22 minutes. 3D DTI experiments were performed with TE = 9.1 ms, TR = 2000 ms, ns = 4, and an EPI factor of 8. Multi-shell diffusion experiments were performed with δ = 1.5 ms, Δ = 4 ms, and an effective b-value range of 100, 1000, or 2500 s/mm^2, with 4, 12, or 24 diffusion-encoding directions, respectively. The FOV was 2.52 × 4.97 × 1.82 mm, with a matrix size of 72 × 142 × 52, resulting in an isotropic resolution of 35 µm and a total scan time of 36 hours, 58 minutes.

Data processing

Brain structure identification. Identification of brain regions and white matter structures was based on various available zebrafish brain atlases and similar sources[29-31]. The cortical thickness of the longitudinal torus (TL), the molecular layer of the cerebellar corpus (CCem), and the optic tectum (TeO) were estimated using the distance measuring tools in Paravision software (Bruker BioSpin GmbH, Germany). The estimation was based on the central sagittal or coronal slice at a b-value of 2500 s/mm^2 from 3D DTI measurements obtained at 17.6 T. The volume of the main brain regions, including the total brain volume, was estimated using Matlab

R2021b (mathworks.com). Raw DTI data was imported into Matlab with a modified version of read_2dseq[32]. The mean intensity of the largest acquired *b*-value was calculated, as it provided the optimal contrast for segmenting the brain into its main regions. The segmentation of brain regions was performed in the Volume Segmenter tool of Matlab, after which their volumes were calculated based on the applied resolution.

Estimation of T_2. The estimation of T_2 was performed using MSME data. Uneven echoes were excluded from the data fitting to compensate for imperfect refocusing pulses[33], and the first 12 remaining echoes (12 – 144 ms) were used for fitting. After 144 ms, the signal-to-noise ratio (SNR) fell below the threshold value for a Gaussian distribution of the T_2 signal (see Supplementary Figure S3.1.), required for reliable line-fitting. T_2 was estimated with a non-linear least square algorithm for the exponential fit function according to

$$I_{\mathrm{TE}} = A + I_0 \cdot \exp^{\frac{-TE}{T_2}} \quad , \tag{3.1}$$

where I_{TE} is the signal intensity at echo time *TE*, *A* is the absolute bias, I_0 is the signal intensity at TE_0, and *TE* is the echo time (ms).

Estimation of *ADC*. The estimation of the apparent diffusion coefficient (*ADC*) was performed from DWI data, with a non-linear least square algorithm for the exponential fit function

$$I_{\mathrm{b}} = A + I_0 \cdot \exp^{-b \cdot ADC} \quad . \tag{3.2}$$

Here I_b is the signal intensity at *b* and I_0 is the signal intensity at time b_0.

***ADC* multi-component analysis by the phasor approach.** Mono- and multi-component *ADC* analysis by the phasor approach was performed using Matlab. Raw DWI data was imported into Matlab. DWI data is transformed to phasor plot coordinates by selecting region of interest (ROI) using the volume segmenter tool. Next, for each individual *ADC* decay curve in the ROI a stepwise approach was followed. (1) An absolute bias systematic error correction was performed, based on a Rayleigh probability distribution fit of the background signal (see Supplementary Figure S3.2.). (2) Next, the data was filtered by an arithmetic mean filter with filter size 2, (3) followed by normalization to the [0, 1] range, (4) fast-Fourier transformation, (5) selection of the first harmonics, and finally (6) plotting the real versus the imaginary part. The semi-circle of the phasor plot, representing the phasor coordinates of mono-component *ADC*, is added for *ADC* between 0 and 0.001 mm^2/s based on Eq.3.2. Mono-component analysis of DWI is performed by projecting the phasor plot coordinates of the ROIs onto the semi-circle using the Matlab dsearchn() function. In addition, a bi-component analysis was performed,

based on the bi-exponential fit function

$$I_{\mathrm{b}} = a \cdot \exp^{-b \cdot ADC_{\mathrm{slow}}} + c \cdot \exp^{-b \cdot ADC_{\mathrm{fast}}} \quad . \tag{3.3}$$

Here *a* and *c* are the areas of component ADC_{slow} and ADC_{fast}, respectively. For this, ADC_{slow} was taken between 0 and $4{\cdot}10^{-4}$ mm^2/s, ADC_{fast} between $4.1{\cdot}10^{-4}$ and $1{\cdot}10^{-3}$ mm^2/s, with a step-size of $1{\cdot}10^{-5}$ mm^2/s, and step-sizes of 1% for *a* and *c*. Obtained values were verified by determining the fit (R^2) using the curve fitting tool in Matlab.

Processing of DTI data. DTI data processing, including diffusion metrics estimation and white matter connectivity analysis by tractography, was conducted using MRtrix3 software[34] and Matlab. Brain masks were generated using the Volume Segmenter tool in Matlab. Raw DTI data was denoised based on the random matrix theory and potential Gibbs ringing artifacts were removed based on the method of local subvoxel-shifts[35], implemented through MRtrix3 functionality[36]. The estimations of the (apparent) diffusions tensors (**D**) and (apparent) diffusion kurtosis tensors (**W**) were also executed through functionalities available within MRtrix3. **D** and **W** were derived from logarithmically transformed and pre-processed DTI data through a two-stage procedure. First, the fitting process employed weighted least-squares methodology, which were based on empirical signal intensities. Second, an iterated weighted least-squares approach was used, utilizing the signal predictions from preceding iteration to inform subsequent iterations. In total, two iterations are performed. Due to their full symmetric, **D** and **W** have 6 and 15 degrees of freedom, respectively. Construction of **W** requires a minimum of 22 diffusion-weighted images taken at 3 distinct *b*-values towards 15 unique diffusion-encoding directions[37]. Full descriptions of the methodology is provided by Basser *et al.* for **D**, and Veraart *et al.* for **W** [38,39]. Diffusion tensor metrics ($D_{\parallel}$, $D_{\perp}$, *MD*, and *FA*) were estimated from **D**, according to

$$D_{\parallel} = \lambda_1 \tag{3.4}$$

$$D_{\perp} = \frac{\lambda_2 + \lambda_3}{2} \tag{3.5}$$

$$MD = \frac{\lambda_1 + \lambda_2 + \lambda_3}{3} \text{ , and} \tag{3.6}$$

$$FA = \frac{\|D - MD \cdot I^{(2)}\|}{\|D\|} = \sqrt{\frac{\frac{3}{2}\left((\lambda_1 - MD)^2 + (\lambda_2 - MD)^2 + (\lambda_3 - MD)^2\right)}{\lambda_1{}^2 + \lambda_2{}^2 + \lambda_3{}^2}} \tag{3.7}$$

The λ_1, λ_2, and λ_3 are the eigenvalues of **D**, arranged such that $\lambda_1 \geq \lambda_2 \geq \lambda_3$, $\mathbf{I}^{(2)}$ is the fully symmetric rank 2 isotropic tensor, and $||..||$ denote the application of the Frobenius norm. For the estimation of the diffusion kurtosis tensor metrics, **W** was utilized[40,41]. Estimation of *MK*

was based on the equation for rapid *MK* estimation as defined by Hansen and Jespersen[42],

$$MK = \frac{1}{5}\mathrm{Tr}(\mathbf{W}) \tag{3.8A}$$

$$MK = \frac{1}{5}\left(W_{1111} + W_{2222} + W_{3333} + 2\,W_{1122} + 2\,W_{1133} + 2\,W_{2233}\right) \tag{3.8B}$$

Where W_{ijkl} are the diffusion kurtosis tensor elements. Estimation of $K_{\parallel}$ was based on

$$K_{\parallel} = \frac{\lambda_1+\lambda_2+\lambda_3}{9\cdot{\lambda_1}^2} W_{1111} \quad . \tag{3.9}$$

Estimation of $K_{\perp}$ was based on

$$K_{\perp} = G_1 W_{2222} + G_1 W_{3333} + G_2 W_{2233} \quad . \tag{3.10}$$

with

$$G_1 = \frac{(\lambda_1+\lambda_2+\lambda_3)^2}{18\lambda_2\cdot(\lambda_2+\lambda_3)^2} \cdot \left(2\lambda_2 + \frac{{\lambda_3}^2 - 3\lambda_2\cdot\lambda_3}{\sqrt{\lambda_2\cdot\lambda_3}}\right) \quad \text{and} \tag{3.11A}$$

$$G_2 = \frac{(\lambda_1+\lambda_2+\lambda_3)^2}{3\cdot(\lambda_2+\lambda_3)^2} \cdot \left(\frac{\lambda_2+\lambda_3}{\sqrt{\lambda_2\cdot\lambda_3}} - 2\right) \quad . \tag{3.11B}$$

The estimation of *KFA* was based on

$$KFA = \frac{||W - MK\cdot I^{(4)}||}{||W||} \quad , \tag{3.12}$$

where $\mathbf{I}^{(4)}$ is the fully symmetric rank 4 isotropic tensor and **W** was formed by permutating its 15 unique elements, which were acquired from MRtrix3 software.

White matter structure identification by DTI tractography. To identify white matter structures in the zebrafish brain, tractography was employed using super-resolution (5 µm) short-track track-density imaging by multi-shell multi-tissue constraint spherical deconvolution (stTDI msmt CSD) conducted using the MRtrix3 software[34]. Estimation of the msmt CSD response functions was performed by the Dhollander algorithm[43], selecting the top 10.0%, 2.0% and 10.0% of refined white matter, grey matter, and cerebrospinal fluid (CSF) voxels, respectively. Crude segmentation of white matter from grey matter and CSF was performed at *FA* = 0.15. Fibre orientation distribution functions (fODFs) were estimated using the msmt-CSD algorithm[44]. Whole brain short track tractography was performed with the iFOD1 algorithm[45], generating 10 million tracks, with a length between two and ten voxels. Generated tracks were converted to super-resolution TDI[46], obtaining connectivity images at an approximate 5 µm resolution, in which the orientation of tracks is indicated by directional encoded colour (DEC).

Statistical analysis. All statistical analysis of data was performed using Matlab and GraphPad Prism version 9.0.0 for Windows, (Graphpad Software, San Diego, California, USA, www.graphpad.com). Test of significance was performed using the unpaired *t*-test, assuming Gaussian distribution, with a p of < 0.05 considered as a significant difference between the two groups. Possible outliers were identified and removed based on three scaled median absolute deviations (MAD) from the median value.

3. RESULTS AND DISCUSSION

In this study, we probed the effect of genomic deletion of TLR2 on microstructural changes observed in the brain of *tlr2*$^{-/-}$ adult zebrafish non-invasively, utilizing state-of-the-art MR imaging at an ultra-high magnetic field strength of 17.6 T.

Changes in brain morphology observed in tlr2*$^{-/-}$ *zebrafish brain.

Figure 3.1 presents high-resolution images of control and *tlr2*$^{-/-}$ male zebrafish, acquired using 3D DTI at a *b*-value of 2500 s/mm^2. DTI offered enhanced contrast compared to conventional anatomical imaging techniques, enabling clear separation of tiny zebrafish brain structures. Differences in the cortical thickness of brain structures were observed in the cerebellum and the mesencephalon (Figure 3.1A). In the cerebellum, the thickness of the molecular layer of the cerebellar corpus (CCem) was found significantly enlarged by approximately 38% in *tlr2*$^{-/-}$ zebrafish compared to the control group (Figure 3.1C). Similar observations were made in the mesencephalon, where the volumes of the longitudinal torus (TL) and optic tectum (OT) were significantly increased by approximately 29% and 27%, respectively. To expand upon pathologically derived differences in brain structure observed in *tlr2*$^{-/-}$ zebrafish, brain volumes were estimated utilizing 3D DTI data. The zebrafish brain was divided into its main regions[29,30]; the olfactory bulb (OB), pallium (Pa), diencephalon (DC), mesencephalon (MC), cerebellum (CB), and rhombencephalon (RC) (Figure 3.1B). In *tlr2*$^{-/-}$ zebrafish, a significant increase in the volume of the CB and RC was observed ($p < 0.05$, $n = 3$) compared to the control group. Our results demonstrate an increase in the cortical thickness and trend toward increased brain volume of the *tlr2*$^{-/-}$ zebrafish compared to the control group, while the differences in body length and weight between three-month old *tlr2*$^{-/-}$ and control zebrafish was negligible (data not shown). Previously, a significant reduction in the cortex thickness, in combination with white matter damage and neuronal loss was reported for TLR2 deficient mice[11]. In addition, *tlr2*$^{-/-}$ was associated with significantly reduced levels of insulin-like growth factor 1 (IGF-1), which has neuroprotective properties and plays an important role in neuronal viability and prevention of apoptosis[47]. While neurodegenerative disorders are typically linked to cortical thinning and reduced brain volumes in their advanced stages, it has been observed that cortical thickening and volumetric increase occur in the initial phases as a reaction to underlying pathological

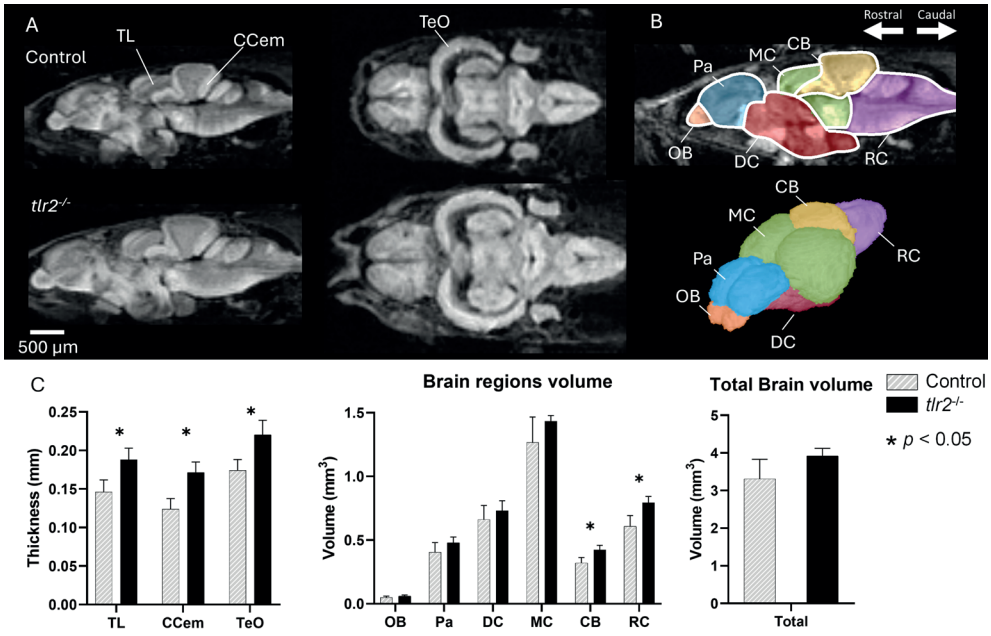

Figure 3.1. Comparison of brain structure and volume in tlr2$^{-/-}$ and control adult zebrafish. [A] *Representative sagittal and coronal slice of DTI of control and tlr2$^{-/-}$adult zebrafish obtained at 17.6 T.* ***[B]*** *2D and 3D representation of the zebrafish brain, divided into its main regions, providing a comprehensive view of its anatomical organisation.* ***[C]*** *Comparison of the cortical thickness of the longitudinal torus (TL), molecular layer of the cerebellar corpus (CCem), and optic tectum (TeO) shows a significant increase in tlr2$^{-/-}$ zebrafish compared to control. Furthermore, a significant increase in the volume of the cerebellum (CB) and rhombencephalon (RC) were observed. In all other brain region, as for the total brain volume, a similar trend is observed, albeit non-significantly ($p > 0.05$). Acquisition details: TR = 2000 ms, TE = 9 ms, ns = 4, isotropic resolution 35 µm, effective b-value range 100, 1000, or 2500 s/mm^2, with 4, 12 or 24 diffusion-encoding directions respectively. TL – Longitudinal torus; CCem – Cerebellar corpus, molecular layer; OB – Olfactory bulb; Pa – Pallium; DC – Diencephalon; MC – Mesencephalon; CB – Cerebellum; RC – Rhombencephalon. Statistical analysis was performed using the unpaired t-test, assuming Gaussian distribution, with $p < 0.05$ considered to imply significant differences between the control and tlr2$^{-/-}$ group.*

processes[48,49]. The observed increase in cortical thickness could be an early indicator of neurodegenerative processes associated with TLR2 deficiency. Furthermore, increase brain volume may be associated with swelling of the brain due to cerebral edema, *i.e.* the abnormal swelling of brain cells by accumulation of fluid. Previous studies in *tlr2*$^{-/-}$ mice have shown hypoperfusion in the brain that could indirectly signify cytotoxic edema[50]. A longitudinal study, outside the scope of the current work, would be required to provide more insight in the development of changes in cortical thickness and brain volume of *tlr2*$^{-/-}$ zebrafish.

T_2 and ADC changes underpinning cytotoxic edema and astrogliosis in tlr2$^{-/-}$ brain.

To zoom into microstructural changes in the zebrafish brain, we utilized T_2 and *ADC* estimation. Previously, quantitative T_2 and *ADC* measurements were used for evaluation of normal and affected brain tissue, including regular ageing, strokes, tumours, and neurodegenerative diseases[51-58]. In this study, prior to conducting T_2 measurements, we examined the potential influence of magnetic field disturbances on estimated T_2 by investigating the impact of the CPMG refocusing pulse interval, as described previously[51]. The influence of pulse intervals between 6 to 18 ms on brain T_2 was negligible (see Supplementary Figure S3.3.), suggesting insignificant impact of magnetic field disturbances on estimated T_2. In addition, the differences in T_2 times between single-slice MSME and multi-slice MSME were also negligible (see Supplementary Figure S3.3.), highlighting a minimal influence of magnetization transfer-related bias of the water signal[59]. Figure 3.2 shows T_2 and *ADC* changes in six areas in control and *tlr2*$^{-/-}$ zebrafish brain. ROIs were selected in various brain regions; the granular layer of the cerebellar corpus (CCeg), the CCem, the TL, the medial longitudinal torus (MLF), the diffusive nucleus of the inferior lobe (DIL), and the medial zone of the dorsal telencephalon (DM). An overall increase in the T_2 relaxation time was observed in all selected brain regions of the *tlr2*$^{-/-}$ zebrafish brain (Figure 3.2B) ranging between 17% in the DM and 28% in the CGeg. Complementary, *ADC* analysis showed a significant reduction of the diffusivity in the CCeg, CCem, and DM by 42%, 39%, and 23%, respectively. Other ROIs showed a similar trend towards reduced diffusivity. The elevation in T_2, coupled with the reduction in *ADC* could be an indication of elevated astrogliosis and astroglia scarring[60,61], as documented in earlier studies for *tlr2*$^{-/-}$ mice[62]. Moreover, in contrast to vasogenic edema which exhibits significant increases in diffusivity, cytotoxic edema results in restricted diffusion and reduced *ADC*[63,64], most profoundly occurring in astrocytes[65]. An increase in potential biomarkers of edema such as aquaporin 4 (AQP4), that regulate brain water and CSF water movement, have been detected in models of neurodegeneration disease [21]. It is intriguing that an increase in cortical thickness in asymptomatic mutation carriers was reported along with a substantial reduction in the mean diffusivity, almost a decade prior to the predicted clinical onset[48], a finding that parallels the alterations in cerebral volume and reduced diffusivity in the current study. In the present work, zebrafish were subjected to formalin fixation to mitigate degradation processes during analysis. In this context, it is noteworthy to acknowledge that formalin fixation might affect T_2 and diffusion characteristics as compared to *in vivo* situation[20,66]. Nevertheless, to get relevant comparison between fixed control and *tlr2*$^{-/-}$ fish, we follow strictly same fixation protocol for both groups. Moreover, formalin fixation shortens T_1 relaxation times, allowing for the use of shorter repetition times compared to those required *in vivo*. This poses a valid challenge when translating our methods for *in vivo* measurements, as longer repetition times would be required, consequently extending total scan times further.

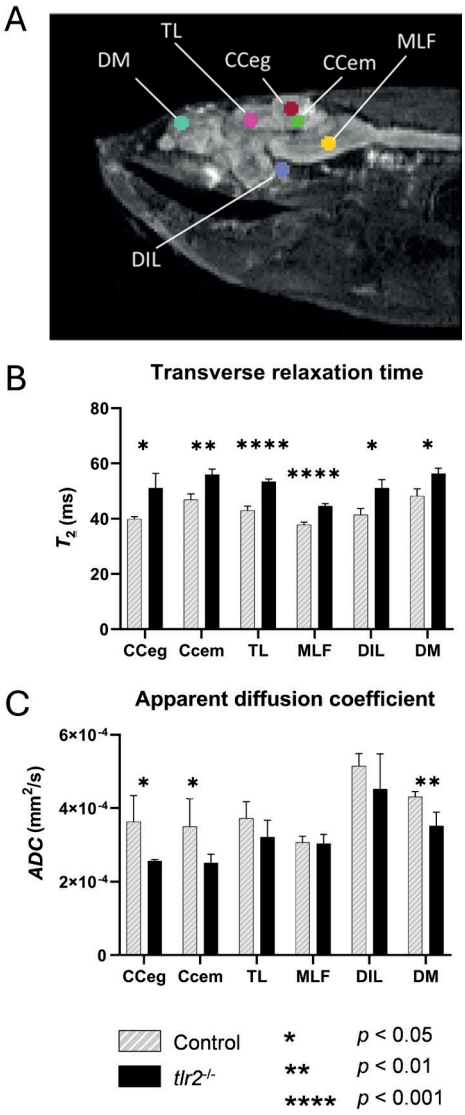

Figure 3.2. T_2 relaxation time and ADC measurement in various brain regions of control and tlr2 mutant (tlr2$^{-/-}$) zebrafish. [A] *Anatomical DWI image (b = 1000 s/mm^2), sagittal slice, showing ROIs used for T_2 and ADC estimation.* ***[B]*** *Estimated T_2 relaxation times in selected ROIs of control and tlr2$^{-/-}$ zebrafish.* ***[C]*** *Estimated ADC in selected ROIs of control and tlr2$^{-/-}$ zebrafish. Acquisition details MSME: TR = 3000, τ = 6.0 ms, ns = 4, resolution 47 × 47 µm, and a slice thickness 500 µm. DWI: TR = 1000 ms, TE = 13 ms, ns = 4, resolution 47 × 47 µm, slice thickness 200 µm, effective b-value range 50, 500, 1000, 1500, 2000, 2500, or 3000 s/mm^2. Statistical analysis was performed using the unpaired t-test, assuming Gaussian distributions, with $p < 0.05$ considered to imply significant differences between the control and tlr2$^{-/-}$ group. * $p < 0.05$, ** $p < 0.01$, **** $p < 0.001$. DM – Medial zone of dorsal telencephalon; TL – Longitudinal torus; Cceg – Granular layer of the cerebellar corpus; Ccem – Molecular layer of the cerebellar corpus; MLF – Medial longitudinal fascicle; DIL – Diffuse nucleus of the inferior lobe.*

Phasor-based multi-component analysis reveals restricted diffusivity in tlr2$^{-/-}$ zebrafish brain.

To obtain further insight in the nature of the observed reduced diffusivity, multi-component analysis of exponential *ADC* decay curves was performed by the phasor approach[67]. *ADC* is influenced by the mobility of water molecules in different tissue compartments, with each compartment exhibiting distinct *ADC* components. Several studies have shown bi-exponential diffusion decay in the brain, characterised by slow and fast diffusion compartments[68-70]. In this context, the slow diffusion component represents compartments within the brain that exhibit hindered diffusion, while the fast diffusion component represents compartments with relatively unrestricted diffusion. Although it has been suggested that these compartments represent intracellular and extracellular populations, there is evidence indicating that both compartments partly originate from the intracellular space[70]. The current work refers to these compartments as slow and fast diffusion components rather than intracellular and extracellular diffusivity. Here, we chose the CCem structure as our prime example for conducting a multi-component *ADC* analysis due to its notable alterations in T_2 and *ADC*. In this context, our emphasis was on exploring the multi-component characteristics of the *ADC* signal within affected brain tissue in *tlr2*$^{-/-}$ zebrafish. Multi-component analysis of the *ADC* decay curve was conducted employing the phasor approach (Figure 3.3). Phasor data from the CCem of *tlr2*$^{-/-}$ and control zebrafish brain demonstrated nearly complete separation (Figure 3.3A), indicating significant differences in the *ADC* of both groups. Figure 3.3B displays the mono-component analysis of *ADC* value changes in the CCem of *tlr2*$^{-/-}$ showing that the *ADC* of *tlr2*$^{-/-}$ was significantly reduced compared to the control group, which is well in line with the results of fitting by the non-linear least square algorithm discussed in Figure 3.2. The shape of the phasor data, fully separated from the semi-circle, indicates a bi-component system with a slow ($0 < ADC_{slow} < 4{\cdot}10^{-4}$ mm^2/s) and a fast ($4{\cdot}10^{-4} < ADC_{fast} < 1{\cdot}10^{-3}$ mm^2/s) *ADC* component. The phasor plot coordinates of the CCem were fitted to bi-component *ADC* systems, based on the bi-exponential fit function [Eq.3]. Mean ADC_{slow} and ADC_{fast} found for the CCem of *tlr2*$^{-/-}$ and control zebrafish by the phasor approach, as well as their area (%) are summarised in Figure 3.3C-E. The bi-component analysis showed a significant reduction in the absolute value of ADC_{fast}, and a substantial increase in the area of ADC_{slow}. These findings imply diffusivity in the CCem of *tlr2*$^{-/-}$ zebrafish is primarily influenced by slow diffusion compartments, to a greater extent than observed in the control group. In addition, they point to microstructural changes occurring within the fast diffusivity compartments. Various biological processes could lead to restricted diffusion. Among these, astrogliosis, cytotoxic edema and inflammatory processes have been previously reported for *tlr2*$^{-/-}$ models, although conflicting reports are available for pro-inflammatory processes in TLR2 deficiency[71,72]. In the current work, we applied very short diffusion encoding times which facilitated exploration of water diffusion over very short distances (micrometre regime), reducing the influence of potential interaction occurring during

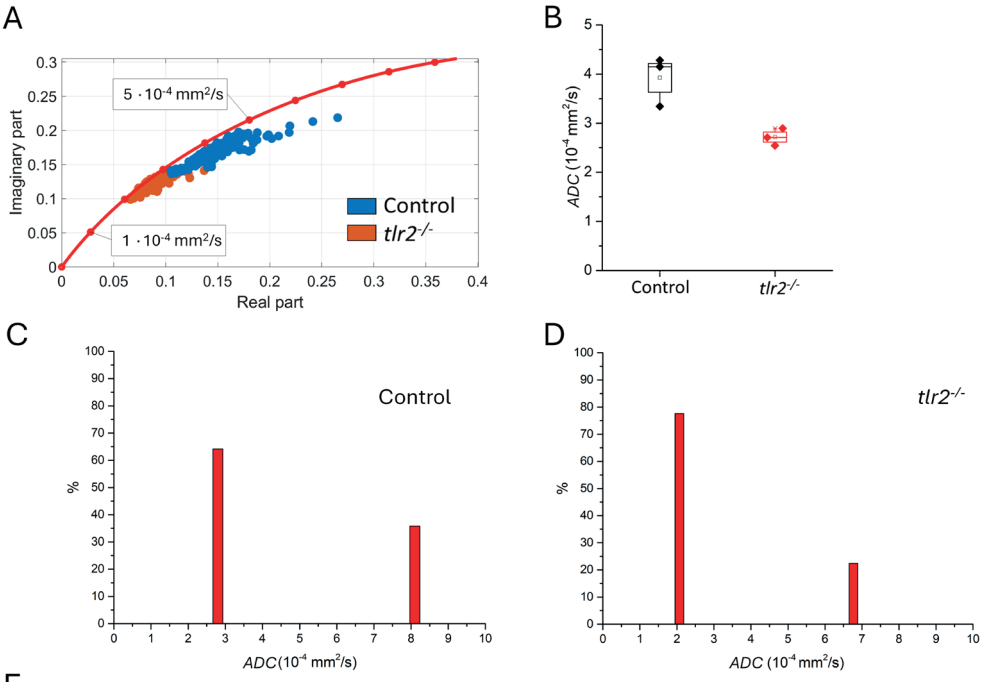

E

	Control		*tlr2*$^{-/-}$	
	ADC ·10^{-4} (mm^2/s)	Area (%)	*ADC* ·10^{-4} (mm^2/s)	Area (%)
Slow component	2.8 ± 0.2	64.2 ± 2.4	2.1 ± 0.0	77.6 ± 2.4*
Fast component	8.1 ± 0.3	35.8 ± 2.4	6.8 ± 0.2*	22.4 ± 2.4*
R^2 of fit	0.9992		0.9993	

Figure 3.3. Phasor analysis of the experimental ADC curves. [A] *Phasor plot of the molecular layer of the cerebellar corpus (Ccem) of tlr2*$^{-/-}$ *and control, relative to the phasor plot semi-circle (red). On the semi-circle, 0 mm*^{2}*/s is located at [0,0], with steps of 1·10*$^{-4}$ *mm*^{2}*/s indicated as red dots on the semi-circle.* ***[B]*** *Mono-component analysis shows the ADC in tlr2*$^{-/-}$ *is significantly reduced, while multi-component analysis of the ADC decay curve in the Ccem* ***[C-E]*** *shows a significant increase in the area of the slow diffusion component in tlr2*$^{-/-}$*, associated with restricted diffusion. Acquisition details DWI used for phasor plot analysis: TR = 1000 ms, TE = 13 ms, ns = 4, resolution 47 × 47 µm, slice thickness 200 µm, effective b-value range 50, 500, 1000, 1500, 2000, 2500, or 3000 s/mm*^{2}*. Statistical analysis was performed using the unpaired t-test, assuming Gaussian distribution, with p < 0.05 considered to imply significant differences between the control and tlr2*$^{-/-}$ *group. * p < 0.05.*

the application of longer diffusion times[73]. The spatial regime achieved in our work may not be currently feasible with clinical system due to lack of strong field gradients.

DTI and DKI analysis reveal diminished diffusivity and enhanced kurtosis in tlr2$^{-/-}$ brain.
To further evaluate potential alterations in the microstructure in *tlr2*$^{-/-}$ zebrafish brain, DTI was utilized. DTI expands upon traditional dMRI. It enhances the understanding of structural characteristics by utilizing the effects of anisotropic diffusion, accessed by measuring the diffusion-weighted MR signal in at least six different diffusion directions. These diffusion-weighted MR signals are translated into a diffusion tensor, represented as an ellipsoid model, of which the eigenvectors ($\boldsymbol{\varepsilon}_1$, $\boldsymbol{\varepsilon}_2$, $\boldsymbol{\varepsilon}_3$) and eigenvalues ($\lambda_1$, λ_2, λ_3) represent the principal axis frame of the diffusion tensor and the diffusivity, respectively. Here, the eigenvectors are arranged such that $\lambda_1 \geq \lambda_2 \geq \lambda_3$. In white matter structures, the diffusivity along the axons is the least restricted and represented by the largest principal eigenvalue, the axial diffusivity ($D_{\shortparallel}$, λ_1). The diffusivity perpendicular to the axons is represented by the average of the eigenvalues λ_2 and λ_3, the radial diffusivity ($D_{\perp}$). The mean diffusivity is estimated as the average intensity of the three eigenvectors (*MD*). Finally, *FA* is used to estimate the extent of the directional preference of the diffusivity, where an *FA* of 0 indicated full isotropic diffusivity and an *FA* of 1 indicates full anisotropic diffusivity. In the current study, DTI data was used to generate $D_{\shortparallel}$, $D_{\perp}$, *MD*, and *FA* maps (Figure 3.4A) and estimate mean $D_{\shortparallel}$, $D_{\perp}$, *MD*, and *FA* of major brain regions (Figure 3.4C).

Differences in $D_{\shortparallel}$, $D_{\perp}$, and *MD* in the major brain region were found negligible, although a robust and consistent trend towards decreased $D_{\shortparallel}$, $D_{\perp}$, and *MD* was observed, aligning closely with the reduced *ADC* found by DWI and previous reports[10]. Notably, *FA* exhibited a significant reduction in the pallium and mesencephalon, in line with earlier observations for *tlr2*$^{-/-}$ mice[11]. In other brain regions, a similar tendency towards reduced *FA* was consistently observed in *tlr2*$^{-/-}$ zebrafish relative to the control group, albeit non-significant.

Further insight was obtained by employing DKI. DWI and DTI rely on the assumption that diffusivity follows a Gaussian distribution, thus simplifying the true complexity of diffusivity in the brain[74]. Considering these limitations, DKI is an extended dMRI technique for the characterisation of non-Gaussian diffusion, describing the kurtosis of the diffusion distribution. To quantify kurtosis, application of higher *b*-values is required as the diffusion signal is mostly influenced by Gaussian diffusion at lower *b*-values[75]. In our findings, we observe the emergence of kurtosis effects at *b*-values exceeding 2000 s/mm^2, and it is increasing at larger *b*-values (see Supplementary Figure S3.4.). DKI data was used to generate $K_{\shortparallel}$, $K_{\perp}$, *MK*, and *KFA* maps (Figure 3.4B) and estimate mean $K_{\shortparallel}$, $K_{\perp}$, *MK*, and *KFA* of major brain regions (Figure 3.4C). We observed a significant increase in $K_{\perp}$ in the rhombencephalon and cerebellum,

and a significant increase in the *MK* of the rhombencephalon of *tlr2*$^{-/-}$ zebrafish compared to the control group. Elevated diffusion kurtosis signify a greater departure from the Gaussian distribution of water molecule diffusion, suggesting an elevated degree of diffusion restriction. These findings are in full agreement with our mono- and multi-component analysis of the *ADC* signal, indicating strongly restricted diffusion.

In general, the diffusion metrics $D_{\parallel}$ and $D_{\perp}$ are indicative of myelin integrity and axonal damage, *MD* is associated with edema and proliferation of cells in neoplastic growth, and *FA* serves as a highly sensitive biomarker for assessing the integrity of white matter. In this context, diminished *FA* was related to loss of neurons, myelin swellings, and severe cytotoxic edema, and reduced *MD* were related to glial cell death and loss[76]. Regarding kurtosis metrics, $K_{\parallel}$ is particularly responsive to intracellular structures, whereas $K_{\perp}$ is influenced by alterations in cellular membranes and myelin layers. *MK*, on the other hand, is more broadly linked to the microstructural complexity of the brain. An increase in *MK* is may be associated with denser cell packing or greater cellular complexity, while a decrease in *MK* may be attributed to a loss of cellular structure[74]. Moreover, diffusion kurtosis metrics provides some advantages over diffusion tensor metrics for their increased sensitivity for isotropic grey matter[77].

Based on our findings in three-month old *tlr2*$^{-/-}$ zebrafish, when compared to a control group, we observed several changes in brain metrics. These include an increased in brain volume, strong T_2 signals, reduced *ADC*, restricted diffusivity, and alterations in various diffusion tensor and diffusion kurtosis metrics, such as diminished $D_{\parallel}$, $D_{\perp}$, *MD*, and *FA*, coupled with an increase in $K_{\parallel}$, $K_{\perp}$, *MK*. Demyelination is typically associated with increased $D_{\perp}$, unadjusted $D_{\parallel}$, reduced *FA*, and decreased $K_{\perp}$ and *MK*[78-80]. Reactive astrogliosis was previously found to lead to decreased $D_{\parallel}$, stable $D_{\perp}$, reduced *MD*, increased *FA*, and increased *MK*[81,82]. Our findings suggest axonal degeneration or cytotoxic edema within the analysed brain regions. For axonal degeneration, reduced $D_{\parallel}$, $D_{\perp}$, and *FA* were reported, with apparent increase of kurtosis[79,83-85]. A decrease in diffusivity ($D_{\parallel}$, $D_{\perp}$, *MD*), decrease in *FA*, and increase in kurtosis ($K_{\parallel}$, $K_{\perp}$, *MK*) was previously observed in early hypoxic-ischemic brain edema[86].

We conducted an examination to assess the impact of *b*-value dependency on the reliability of estimated diffusion tensor and diffusion kurtosis metrics. Our study extends previous research conducted in single and double shell DTI and DKI measurements[87], whereas we employed triple shell DTI and DKI at ultra-high magnetic field strengths (see Supplementary Figure S3.5.). Upon analysis, we observed the majority of diffusion tensor and diffusion kurtosis metrics did not exhibit a significant shift in response to significant changes in the *b*-value range. This suggests that the majority of diffusion tensor and diffusion kurtosis metrics, obtained at ultra-high magnetic fields and with four distinct *b*-values (b_0 included), are robust and

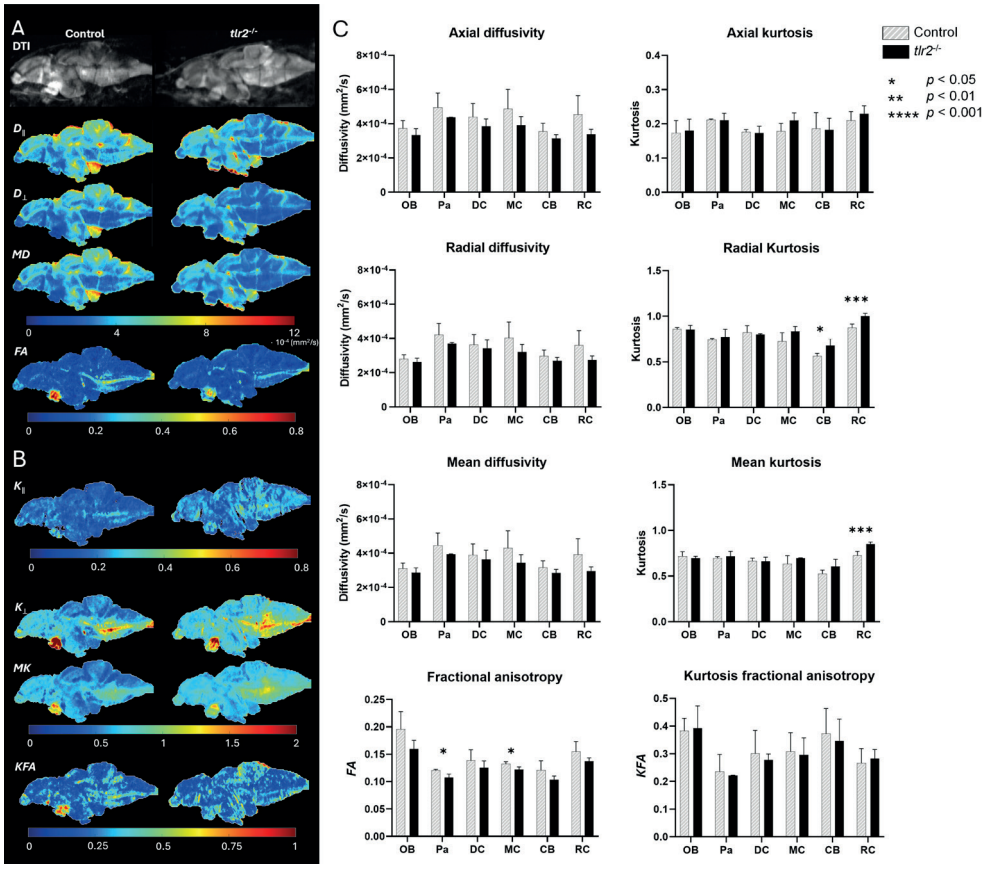

Figure 3.4. Comparison of DTI result in main brain regions of tlr2$^{-/-}$ and control adult zebrafish. *Representative central slice of DTI measurements of control and tlr2$^{-/-}$ adult zebrafish.* ***[A]*** *From these slices, the diffusion tensor metrics were estimated; $D_{\parallel}$, $D_{\perp}$, MD, and FA,* ***[B]*** *as well as the diffusion kurtosis metrics; $K_{\parallel}$, $K_{\perp}$, MK, and KFA.* ***[C]*** *DTI and DKI results of tlr2$^{-/-}$ adult zebrafish compared to controls reveals a noteworthy trend towards decreased $D_{\parallel}$, $D_{\perp}$, and MD, reduced FA, as well as increased $K_{\parallel}$, $K_{\perp}$, and MK. Additionally, a significant decrease in KFA is observed in the tlr2$^{-/-}$ group. Acquisition details: TR = 2000 ms, TE = 12.4 ms, ns = 32, resolution 25 µm × 25 µm × 200 µm, effective b-value range 4, 1000, 3500, or 6000 s/mm2, with 8, 12, 24, or 36 diffusion-encoding directions respectively. Statistical analysis was performed using the unpaired t-test, assuming Gaussian distribution, with $p < 0.05$ considered to imply significant differences between the control and tlr2$^{-/-}$ group. * $p < 0.05$, *** $p < 0.005$. OB – Olfactory bulb; Pa – Pallium; DC – Diencephalon; MC – Mesencephalon; CB – Cerebellum; RC – Rhombencephalon.*

relatively unaffected by variations in the *b*-value range. Based on these findings, we conclude future studies with somewhat similar *b*-value ranges may therefore find our data a valuable reference point.

Genomic deletion of TLR2 signifies compromised integrity in white matter tracks.
Subsequently, we investigated the effect of genomic deletion of TLR2 on white matter integrity in adult zebrafish by DTI. Seven white matter structures were identified and localized in the zebrafish brain using dMRI tractography by stTDI CSD (Figure 3.5A); the posterior commissure (Cpost), the commissure of the secondary gustatory nuclei (Cgus), the ansulate commissure (Cans), the ventral rhombencephalic commissure (Cven), the medial longitudinal fascicle (MLF), the optic tract (OT), and the lateral longitudinal fascicle (LLF). The integrity of these white matter structures was monitored by comparing DTI and DKI metrics. Significantly lower $D_{\shortparallel}$, *MD* and *FA* were observed in the Cven of *tlr2*$^{-/-}$ zebrafish, along with increased $K_{\shortparallel}$, $K_{\perp}$, *MK*, and *FKA*. In the Cgus, we observed a significantly lower *FA* and increased $K_{\perp}$. In addition, the Cpost showed reduced $D_{\shortparallel}$ and *MD*, with increased $K_{\perp}$, the MLF showed increased $K_{\perp}$, and for the LLF reduced $D_{\shortparallel}$, $D_{\perp}$, and *MD*, in combination with increased $K_{\perp}$, and *MK* are reported. Overall, DTI and DKI data of white matter structures in *tlr2*$^{-/-}$ zebrafish shows a consistent trend of reduced diffusivity ($D_{\shortparallel}$, $D_{\perp}$, and *MD*) and *FA* across most white matter structures. Moreover, we observed a trend indicating increased kurtosis ($K_{\shortparallel}$, $K_{\perp}$, and *MK*) and *KFA* when compared to the control group. Previously, increased kurtosis, in combination with decreased diffusivity levels and reduced *FA*, have been attributed to microstructural changes in the brain. APP/PS1 Alzheimer's disease mouse models show a significant increase in kurtosis in the hippocampus, cortex and thalamus, linked to significant increase in amyloid beta (Aβ) plaque loads[88]. A longitudinal report of the same pathological model showed similar observations, including significant drops in *FA* in various brain regions[89]. It has been suggested that TLR2 plays a significant role in clearing toxic Aβ, shown in an APP Alzheimer's disease mouse model[90]. Another observation made in *tlr2*$^{-/-}$ mouse models was increased astrogliosis and demyelination in white matter structures[62]. On the other hand, cuprizone-induced demyelination and inflammation reduced $K_{\shortparallel}$, $K_{\perp}$, and *MK* in the cortex and corpus callosum[80], contrary to the observations in the current study. Increased mean kurtosis was reported as a potential biomarker of reactive astrogliosis, although the same report did not see any significant alterations in *FA* or *MD*[82].

Our analysis has revealed compelling evidence of a compromise in the integrity of various white matter structures within the brain of *tlr2*$^{-/-}$ zebrafish. The alterations of the neural architecture suggest a potential link to neurobehavioral changes observed in other *tlr2*$^{-/-}$ models. Here, we found evidence for microstructural changes in the Cven, a bundle of nerves carrying signals between the two halves of the hind brain. These signals originate from different parts of the brain, including the sensory area for touch and balance, as well as groups of cells related to sensing and moving[91]. Lampreys (*Lampetra fluviatilis*) with a transected Cven exhibited compromised spontaneous locomotion and altered movements[91], illustrating the role played by the Cven in orchestrating and regulating these motor behaviours. These observations are consistent with the diminished spontaneous activity observed in *tlr2*$^{-/-}$

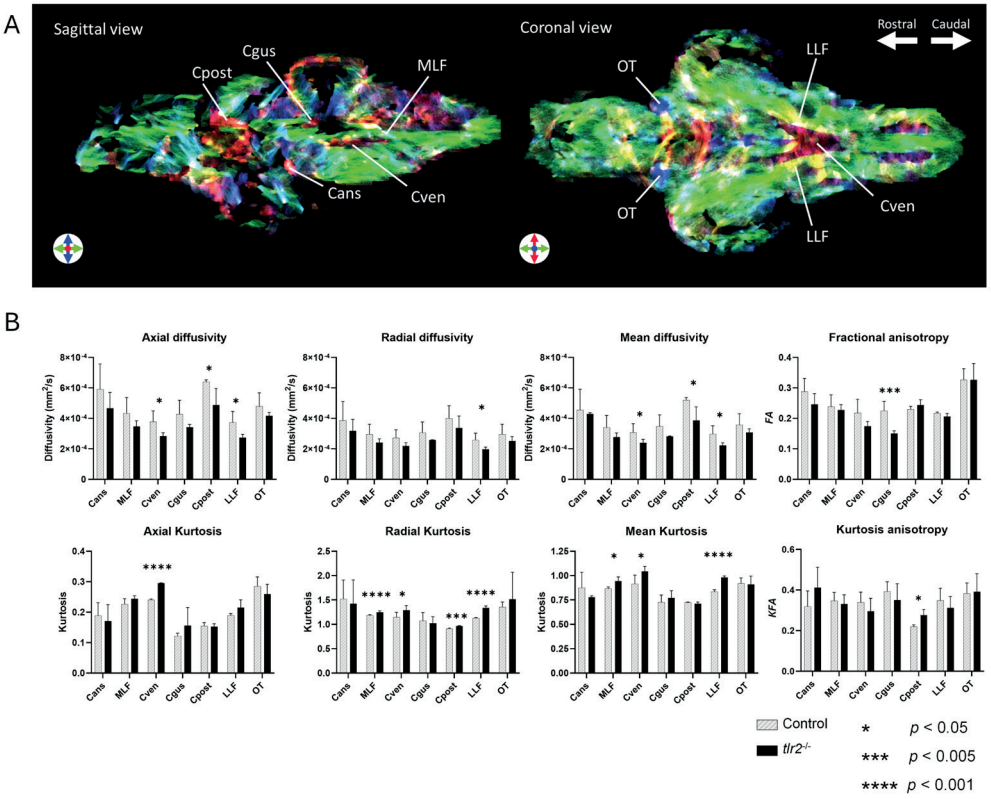

Figure 3.5. Comparison of DTI results of white matter structures of tlr2$^{-/-}$ and control adult zebrafish. [A] *Sagittal and coronal slice of DEC stTDI msmt-CSD map, used for the identification of white matter structures in the zebrafish brain. Acquisition details: TR = 2000 ms, TE = 9 ms, ns = 4, isotropic resolution 35 µm, effective b-value range 100, 1000, or 2500 s/mm^2, with 4, 12, or 24 diffusion-encoding directions respectively.* ***[B]*** *Diffusion metrics estimated by DTI results, show reduced $D_{\parallel}$, $D_{\perp}$, and MD, reduced FA, increased $K_{\parallel}$, $K_{\perp}$, and MK and KFA anisotropy in white matter structures in the tlr2$^{-/-}$ zebrafish brain. Acquisition details: TR= 2000 ms, TE = 12.4 ms, ns = 32, resolution 25 µm × 25 µm × 200 µm, effective b-value range 4, 1000, 3500, or 6000 s/mm2, with 8, 12, 24, or 36 diffusion-encoding directions respectively. Cpost – posterior commissure; Cgus – commissure of the secondary gustatory nuclei; Cans – ansulate commissure; Cven – ventral rhombencephalic commissure; MLF – medial longitudinal fascicle; OT – optic tract; LLF – lateral longitudinal fascicle. Statistical analysis was performed using the unpaired t-test, assuming Gaussian distribution, with p < 0.05 considered to imply significant differences between the control and tlr2$^{-/-}$ group. * p < 0.05, *** p < 0.005, **** p < 0.001.*

mice[11]. Our insight into microstructural alterations in the Cven of *tlr2*$^{-/-}$ zebrafish shed light on this phenomenon. Parallel to the Cven, the Cgus was found affected in *tlr2*$^{-/-}$ zebrafish. The Cgus is the neural pathway connecting the secondary gustatory nuclei present on both sides of the zebrafish brain, which are involved in processing taste-related information as part of the gustatory system[92]. Our observations in microstructural changes in the Cgus could contribute to explaining previous observations in *tlr2*$^{-/-}$ mice, showing diminished food consumption[93], as disrupted communication with the secondary gustatory nuclei might lead to difficulties in processing and perceiving taste sensation. The Cpost is a diencephalic nerve bundle, involved in facilitating communication with the pretectal nuclei[30], involved in visual processing, circadian rhythms and motor control[94]. Previous studies showed disrupted circadian rhythms in *tlr2*$^{-/-}$ mice[93], to which our observations might provide further insight.

4. CONCLUSION AND FUTURE OUTLOOK

In summary, our study unveils the impact of genomic TLR2 deletion in zebrafish, leading to microstructural alterations within diverse brain tissues. Applying dMRI at ultra-high magnetic fields provided the necessary SNR and contrast that has enabled us to discriminate and characterise major brain regions as well as specific white matter structures, thereby unravelling the microstructural changes associated with *tlr2*$^{-/-}$ zebrafish. Distinct dMRI techniques provided a diverse array of diffusion metrics, each offering a unique perspective into the architectural framework and transformations occurring in the pathological model. Notably, our study showed significant changes in the diffusivity and kurtosis profiles of multiple white matter structures, which mirror neurobehavioral shifts observed in *tlr2*$^{-/-}$ models. These findings contribute an additional layer of insight to improve our understanding of the origin of these behavioural changes.

In future, to extrapolate our results to a broader context, research should prioritize replicating these findings with a larger sample size, encompassing both male and female zebrafish across various age groups, including older fish. This approach will facilitate more robust statistical analyses and thorough exploration of potential variables and interactions. Furthermore, techniques such as histological staining and spectroscopic methods including localized spectroscopy and high-resolution magic angle spinning, could offer further insight towards increased understanding of the precise microstructural and metabolic changes in the brain of *tlr2*$^{-/-}$ models. In essence, our research provides insight on the relation between TLR2 and the microstructural architecture of the brain. Especially, our utilization of diffusion MRI at ultra-high magnetic fields signifies a substantial advancement, finally providing the required foundation for investigating these relationships in the tiny zebrafish brain.

ACKNOWLEDGEMENTS

Experiments at the 17.6 T instrument were supported by the uNMR-NL Grid: A distributed, state-of-the-art Magnetic Resonance facility for the Netherlands (NWO grant 184.032.207). The authors thank Karthick Sai Sankar Gupta, Fons Lefeber, and Maria Nardella for technical help provided at the 17.6 T instrument, and Volker Lehmann, Antonios Papaioannou, and Thomas Oerther from Bruker for help troubleshooting and their assistance during the experimental design.

REFERENCES

1 Li, D. & Wu, M. Pattern recognition receptors in health and diseases. *Signal Transduct Target Ther* **6**, 291 (2021). https://doi.org/10.1038/s41392-021-00687-0

2 Hu, W. & Spaink, H. P. The Role of TLR2 in Infectious Diseases Caused by Mycobacteria: From Cell Biology to Therapeutic Target. *Biology (Basel)* **11** (2022). https://doi.org/10.3390/biology11020246

3 Sameer, A. S. & Nissar, S. Toll-Like Receptors (TLRs): Structure, Functions, Signaling, and Role of Their Polymorphisms in Colorectal Cancer Susceptibility. *Biomed Res Int* **2021**, 1157023 (2021). https://doi.org/10.1155/2021/1157023

4 Behzadi, P., Garcia-Perdomo, H. A. & Karpinski, T. M. Toll-Like Receptors: General Molecular and Structural Biology. *J Immunol Res* **2021**, 9914854 (2021). https://doi.org/10.1155/2021/9914854

5 Meijer, A. H. *et al.* Expression analysis of the Toll-like receptor and TIR domain adaptor families of zebrafish. *Mol Immunol* **40**, 773-783 (2004). https://doi.org/10.1016/j.molimm.2003.10.003

6 Oliveira-Nascimento, L., Massari, P. & Wetzler, L. M. The Role of TLR2 in Infection and Immunity. *Front Immunol* **3**, 79 (2012). https://doi.org/10.3389/fimmu.2012.00079

7 Dasu, M. R. *et al.* TLR2 expression and signaling-dependent inflammation impair wound healing in diabetic mice. *Lab Invest* **90**, 1628-1636 (2010). https://doi.org/10.1038/labinvest.2010.158

8 Marks, K. E., Cho, K., Stickling, C. & Reynolds, J. M. Toll-like Receptor 2 in Autoimmune Inflammation. *Immune Netw* **21**, e18 (2021). https://doi.org/10.4110/in.2021.21.e18

9 Pascual, M. *et al.* Toll-like receptors in neuroinflammation, neurodegeneration, and alcohol-induced brain damage. *IUBMB Life* **73**, 900-915 (2021). https://doi.org/10.1002/iub.2510

10 McDonald, C. L. *et al.* Inhibiting TLR2 activation attenuates amyloid accumulation and glial activation in a mouse model of Alzheimer's disease. *Brain Behav Immun* **58**, 191-200 (2016). https://doi.org/10.1016/j.bbi.2016.07.143

11 Zhou, C. *et al.* Genomic deletion of TLR2 induces aggravated white matter damage and deteriorated neurobehavioral functionsin mouse models of Alzheimer's disease. *Aging* **11** (2019). https://doi.org/10.18632/aging.102260

12 Hu, Y. *et al.* Toll-like receptor-2 gene knockout results in neurobehavioral dysfunctions and multiple brain structural and functional abnormalities in mice. *Brain Behav Immun* **91**, 257-266 (2021). https://doi.org/10.1016/j.bbi.2020.10.004

13 van Schadewijk, R. *et al.* Magnetic Resonance Microscopy at Cellular Resolution and Localised Spectroscopy of Medicago truncatula at 22.3 Tesla. *Sci Rep* **10**, 971 (2020). https://doi.org/10.1038/s41598-020-57861-7

14 Kabli, S., Alia, A., Spaink, H. P., Verbeek, F. J. & De Groot, H. J. Magnetic resonance microscopy of the adult zebrafish. *Zebrafish* **3**, 431-439 (2006). https://doi.org/10.1089/zeb.2006.3.431

15 Kabli, S., Spaink, H. P., De Groot, H. J. & Alia, A. In vivo metabolite profile of adult zebrafish brain obtained by high-resolution localized magnetic resonance spectroscopy. *J Magn Reson Imaging* **29**, 275-281 (2009). https://doi.org/10.1002/jmri.21609

16 Haud, N. *et al.* rnaset2 mutant zebrafish model familial cystic leukoencephalopathy and reveal a role for RNase T2 in degrading ribosomal RNA. *Proc Natl Acad Sci U S A* **108**, 1099-1103 (2011). https://doi.org/10.1073/pnas.1009811107

17 Ramirez, I. B. *et al.* Impaired neural development in a zebrafish model for Lowe syndrome. *Hum Mol Genet* **21**, 1744-1759 (2012). https://doi.org/10.1093/hmg/ddr608

18 Kabli, S. *et al.* In vivo magnetic resonance imaging to detect malignant melanoma in adult zebrafish. *Zebrafish* **7**, 143-148 (2010). https://doi.org/10.1089/zeb.2009.0649

19 Eeza, M. N. H. *et al.* Probing microstructural changes in muscles of leptin-deficient zebrafish by non-invasive ex-vivo magnetic resonance microimaging. *PLoS One* **18**, e0284215 (2023). https://doi.org/10.1371/journal.pone.0284215

20 Hamilton, N., Allen, C. & Reynolds, S. Longitudinal MRI brain studies in live adult zebrafish. *NMR Biomed* **36**, e4891 (2023). https://doi.org/10.1002/nbm.4891

21 Gatto, R. G. *et al.* Ultra-High Field Diffusion MRI Reveals Early Axonal Pathology in Spinal Cord of ALS mice. *Transl Neurodegener* **7**, 20 (2018). https://doi.org/10.1186/s40035-018-0122-z

22 Gatto, R. G. & Wu, Y. C. Editorial: Innovative Imaging Techniques in Preclinical Models of Neurodegenerative Diseases. *Front Neurosci* **15**, 801037 (2021). https://doi.org/10.3389/fnins.2021.801037

23 Ullmann, J. F., Calamante, F., Collin, S. P., Reutens, D. C. & Kurniawan, N. D. Enhanced characterization of the zebrafish brain as revealed by super-resolution track-density imaging. *Brain Struct Funct* **220**, 457-468 (2015). https://doi.org/10.1007/s00429-013-0667-7

24 Hu, W. *et al.* Infection and RNA-seq analysis of a zebrafish tlr2 mutant shows a broad function of this toll-like receptor in transcriptional and metabolic control and defense to Mycobacterium marinum infection. *BMC Genomics* **20**, 878 (2019). https://doi.org/10.1186/s12864-019-6265-1

25 Hu, W. *et al.* A Novel Function of TLR2 and MyD88 in the Regulation of Leukocyte Cell Migration Behavior During Wounding in Zebrafish Larvae. *Front Cell Dev Biol* **9**, 624571 (2021). https://doi.org/10.3389/fcell.2021.624571

26 Iglesias, J. E. *et al.* Effect of Fluorinert on the Histological Properties of Formalin-Fixed Human Brain Tissue. *J Neuropathol Exp Neurol* **77**, 1085-1090 (2018). https://doi.org/10.1093/jnen/nly098

27 Carr, H. Y. & Purcell, E. M. Effects of Diffusion on Free Precession in Nuclear Magnetic Resonance Experiments. *Physical Review* **94**, 630-638 (1954). https://doi.org/10.1103/PhysRev.94.630

28 Stejskal, E. O. & Tanner, J. E. Spin Diffusion Measurements: Spin Echoes in the Presence of a Time-Dependent Field Gradient. *The Journal of Chemical Physics* **42**, 288-292 (1965). https://doi.org/10.1063/1.1695690

29 Kenney, J. W. *et al. A 3D adult zebrafish brain atlas (AZBA) for the digital age*, <http://azba.wayne.edu/> (2021).

30 Wullimann, M. F., Rupp, B. & Reichert, H. *Neuroanatomy of the zebrafish brain A topological atlas*. (1996).

31 Haynes, E. M., Ulland, T. K. & Eliceiri, K. W. A Model of Discovery: The Role of Imaging Established and Emerging Non-mammalian Models in Neuroscience. *Front Mol Neurosci* **15**, 867010 (2022). https://doi.org/10.3389/fnmol.2022.867010

32 read_2dseq :Quickly Reads Bruker's 2dseq MRI Images v. 1.0.1 (Mathworks, MATLAB Central File Exchange, 2020).

33 Milford, D., Rosbach, N., Bendszus, M. & Heiland, S. Mono-Exponential Fitting in T2-Relaxometry: Relevance of Offset and First Echo. *PLoS One* **10**, e0145255 (2015). https://doi.org/10.1371/journal.pone.0145255

34 Tournier, J. D. *et al.* MRtrix3: A fast, flexible and open software framework for medical image processing and visualisation. *Neuroimage* **202**, 116137 (2019). https://doi.org/10.1016/j.neuroimage.2019.116137

35 Kellner, E., Dhital, B., Kiselev, V. G. & Reisert, M. Gibbs-ringing artifact removal based on local subvoxel-shifts. *Magn Reson Med* **76**, 1574-1581 (2016). https://doi.org/10.1002/mrm.26054

36 Veraart, J., Fieremans, E. & Novikov, D. S. Diffusion MRI noise mapping using random matrix theory. *Magn Reson Med* **76**, 1582-1593 (2016). https://doi.org/10.1002/mrm.26059

37 Collier, Q. *Robust estimation of diffusion tensor and diffusion kurtosis imagingparameters* PhD thesis, Universiteit Antwerpen, (2018).

38 Basser, P. J., Mattiello, J. & Lebihan, D. Estimation of the Effective Self-Diffusion Tensor from the NMR Spin Echo. *Journal of Magnetic Resonance* **B**, 8 (1994). https://doi.org/https://doi.org/10.1006/jmrb.1994.1037.

39 Veraart, J., Sijbers, J., Sunaert, S., Leemans, A. & Jeurissen, B. Weighted linear least squares estimation of diffusion MRI parameters: strengths, limitations, and pitfalls. *Neuroimage* **81**, 335-346 (2013). https://doi.org/10.1016/j.neuroimage.2013.05.028

40 Hansen, B. & Jespersen, S. N. Kurtosis fractional anisotropy, its contrast and estimation by proxy. *Sci Rep* **6**, 23999 (2016). https://doi.org/10.1038/srep23999

41 Tabesh, A., Jensen, J. H., Ardekani, B. A. & Helpern, J. A. Estimation of tensors and tensor-derived measures in diffusional kurtosis imaging. *Magn Reson Med* **65**, 823-836 (2011). https://doi.org/10.1002/mrm.22655

42 Hansen, B. & Jespersen, S. N. Recent Developments in Fast Kurtosis Imaging. *Frontiers in Physics* **5** (2017). https://doi.org/10.3389/fphy.2017.00040

43 Dhollander, T., Raffelt, D., Mito, R. & Connelly, A. Improved white matter response function estimation for 3-tissue constrained spherical deconvolution. *Conference Paper* (2019).

44 Jeurissen, B., Tournier, J. D., Dhollander, T., Connelly, A. & Sijbers, J. Multi-tissue constrained spherical deconvolution for improved analysis of multi-shell diffusion MRI data. *Neuroimage* **103**, 411-426 (2014). https://doi.org/10.1016/j.neuroimage.2014.07.061

45 Tournier, J. D., Calamante, F. & Connelly, A. MRtrix: Diffusion tractography in crossing fiber regions. *International Journal of Imaging Systems and Technology* **22**, 53-66 (2012). https://doi.org/10.1002/ima.22005

46 Calamante, F., Tournier, J. D., Jackson, G. D. & Connelly, A. Track-density imaging (TDI): super-resolution white matter imaging using whole-brain track-density mapping. *Neuroimage* **53**, 1233-1243 (2010). https://doi.org/10.1016/j.neuroimage.2010.07.024

47 Bohacek, I. *et al.* Toll-like receptor 2 deficiency leads to delayed exacerbation of ischemic injury. *Journal of Neuroinflammation* **9**, 17 (2012). https://doi.org/https://doi.org/10.1186/1742-2094-9-191

48 Fortea, J. *et al.* Increased cortical thickness and caudate volume precede atrophy in PSEN1 mutation carriers. *J Alzheimers Dis* **22**, 909-922 (2010). https://doi.org/10.3233/JAD-2010-100678

49 Espeseth, T. *et al.* Accelerated age-related cortical thinning in healthy carriers of apolipoprotein E epsilon 4. *Neurobiol Aging* **29**, 329-340 (2008). https://doi.org/10.1016/j.neurobiolaging.2006.10.030

50 Kang, K. *et al.* Abnormal cortical thickening and thinning in idiopathic normal-pressure hydrocephalus. *Sci Rep* **10**, 21213 (2020). https://doi.org/10.1038/s41598-020-78067-x

51 Roy, U. *et al.* Degeneration of the suprachiasmatic nucleus in an Alzheimer's disease mouse model monitored by in vivo magnetic resonance relaxation measurements and immunohistochemistry. *J Alzheimers Dis* **69**, 363-375 (2019). https://doi.org/10.3233/JAD-190037

52 Kara, F. *et al.* In vivo measurement of transverse relaxation time in the mouse brain at 17.6 T. *Magn Reson Med* **70**, 985-993 (2013). https://doi.org/10.1002/mrm.24533

53 Ndengera, M. *et al.* Relaxation time of brain tissue in the elderly assessed by synthetic MRI. *Brain Behav* **12**, e2449 (2022). https://doi.org/10.1002/brb3.2449

54 Gideon, P., Thomsen, C. & Henriksen, O. Increased self-diffusion of brain water in normal aging. *J Magn Reson Imaging* **4**, 185-188 (1994). https://doi.org/10.1002/jmri.1880040216

55 Knight, M. J. *et al.* Determining T2 relaxation time and stroke onset relationship in ischaemic stroke within apparent diffusion coefficient-defined lesions. A user-independent method for quantifying the impact of stroke in the human brain. *Biomed Spectrosc Imaging* **8**, 11-28 (2019). https://doi.org/10.3233/bsi-190185

56 McGarry, B. L. *et al.* A Comparison of T(2) Relaxation-Based MRI Stroke Timing Methods in Hyperacute Ischemic Stroke Patients: A Pilot Study. *J Cent Nerv Syst Dis* **12**, 1179573520943314 (2020). https://doi.org/10.1177/1179573520943314

57 Chatel, M., Darcel, F., Certaines de, J., Benoist, L. & Bernard, A. M. T1 and T2 Proton Nuclear Magnetic Resonance (N.M.R.) relaxation times in vitro and human intracranial tumours *Journal of Neuro-Oncology* **3**, 7 (1986).

58 Maier, S. E., Sun, Y. & Mulkern, R. V. Diffusion imaging of brain tumors. *NMR Biomed* **23**, 849-864 (2010). https://doi.org/10.1002/nbm.1544

59 Radunsky, D. *et al.* Analysis of magnetization transfer (MT) influence on quantitative mapping of T(2) relaxation time. *Magn Reson Med* **82**, 145-158 (2019). https://doi.org/10.1002/mrm.27704

60 Lee, D. *et al.* Longer T(2) relaxation time is a marker of hypothalamic gliosis in mice with diet-induced obesity. *Am J Physiol Endocrinol Metab* **304**, E1245-1250 (2013). https://doi.org/10.1152/ajpendo.00020.2013

61 Schroeter, M., Franke, C., Stoll, G. & Hoehn, M. Dynamic changes of magnetic resonance imaging abnormalities in relation to inflammation and glial responses after photothrombotic cerebral infarction in the rat brain. *Acta Neuropathol* **101**, 114-122 (2001). https://doi.org/10.1007/s004010000262

62 Kigerl, K. A. *et al.* Toll-like receptor (TLR)-2 and TLR-4 regulate inflammation, gliosis, and myelin sparing after spinal cord injury. *J Neurochem* **102**, 37-50 (2007). https://doi.org/10.1111/j.1471-4159.2007.04524.x

63 Goyal, M., Sinha, S., Ravishankar, S. & Shivshankar, J. Case report: Reversible restricted diffusion and cytotoxic edema in the perilesional zone following continuous partial seizures. *Indian Journal of Radiology and Imaging* **18** (2008).

64 Koch, S., Rabinstein, A., Falcone, S. & Forteza, A. Diffusion-weighted Imaging Shows Cytotoxic and Vasogenic Edema in Eclampsia. *American Journal of Neuroradiology* **22** (2001).

65 Rosenblum, W. I. Cytotoxic Edema: Monitoring Its Magnitude and Contribution to Brain Swelling. *Journal of Neuropathology & Experimental Neurology* **66** (2007).

66 Shepherd, T. M., Thelwall, P. E., Stanisz, G. J. & Blackband, S. J. Aldehyde fixative solutions alter the water relaxation and diffusion properties of nervous tissue. *Magn Reson Med* **62**, 26-34 (2009). https://doi.org/10.1002/mrm.21977

67 Vergeldt, F. J. *et al.* Multi-component quantitative magnetic resonance imaging by phasor representation. *Sci Rep* **7**, 861 (2017). https://doi.org/10.1038/s41598-017-00864-8

68 Clark, C. A. & Le Bihan, D. Water diffusion compartmentation and anisotropy at high b values in the human brain. *Magnetic Resonance in Medicine* **44**, 852-859 (2000). https://doi.org/10.1002/1522-2594(200012)44:6<852::Aid-mrm5>3.0.Co;2-a

69 Mulkern, R. V. *et al.* Multi-component apparent diffusion coefficients in human brain. *NMR in Biomedicine* **12**, 51-62 (1999). https://doi.org/10.1002/(sici)1099-1492(199902)12:1<51::Aid-nbm546>3.0.Co;2-e

70 Sehy, J. V., Ackerman, J. J. & Neil, J. J. Evidence that both fast and slow water ADC components arise from intracellular space. *Magn Reson Med* **48**, 765-770 (2002). https://doi.org/10.1002/mrm.10301

71 Echchannaoui, H. *et al.* Toll-like receptor 2-deficient mice are highly susceptible to Streptococcus pneumoniae meningitis because of reduced bacterial clearing and enhanced inflammation. *J Infect Dis* **186**, 798-806 (2002). https://doi.org/10.1086/342845

72 Winters, L. *et al.* Expression analysis of genes involved in TLR2-related signaling pathway: Inflammation and apoptosis after ischemic brain injury. *Neuroscience* **238**, 87-96 (2013). https://doi.org/10.1016/j.neuroscience.2013.02.001

73 Pyatigorskaya, N., Le Bihan, D., Reynaud, O. & Ciobanu, L. Relationship between the diffusion time and the diffusion MRI signal observed at 17.2 Tesla in the healthy rat brain cortex. *Magn Reson Med* **72**, 492-500 (2014). https://doi.org/10.1002/mrm.24921

74 Steven, A. J., Zhuo, J. & Melhem, E. R. Diffusion kurtosis imaging: an emerging technique for evaluating the microstructural environment of the brain. *AJR Am J Roentgenol* **202**, W26-33 (2014). https://doi.org/10.2214/AJR.13.11365

75 Jensen, J. H., Helpern, J. A., Ramani, A., Lu, H. & Kaczynski, K. Diffusional kurtosis imaging: the quantification of non-gaussian water diffusion by means of magnetic resonance imaging. *Magn Reson Med* **53**, 1432-1440 (2005). https://doi.org/10.1002/mrm.20508

76 Lee, J. K. *et al.* Fractional anisotropy from diffusion tensor imaging correlates with acute astrocyte and myelin swelling in neonatal swine models of excitotoxic and hypoxic-ischemic brain injury. *J Comp Neurol* **529**, 2750-2770 (2021). https://doi.org/10.1002/cne.25121

77 Jensen, J. H. *et al.* Preliminary observations of increased diffusional kurtosis in human brain following recent cerebral infarction. *NMR Biomed* **24**, 452-457 (2011). https://doi.org/10.1002/nbm.1610

78 Song, S. K. *et al.* Dysmyelination revealed through MRI as increased radial (but unchanged axial) diffusion of water. *Neuroimage* **17**, 1429-1436 (2002). https://doi.org/10.1006/nimg.2002.1267

79 Andersen, K. W. *et al.* Disentangling white-matter damage from physiological fibre orientation dispersion in multiple sclerosis. *Brain Commun* **2**, fcaa077 (2020). https://doi.org/10.1093/braincomms/fcaa077

80 Guglielmetti, C. *et al.* Diffusion kurtosis imaging probes cortical alterations and white matter pathology following cuprizone induced demyelination and spontaneous remyelination. *Neuroimage* **125**, 363-377 (2016). https://doi.org/10.1016/j.neuroimage.2015.10.052

81 Budde, M. D., Janes, L., Gold, E., Turtzo, L. C. & Frank, J. A. The contribution of gliosis to diffusion tensor anisotropy and tractography following traumatic brain injury: validation in the rat using Fourier analysis of stained tissue sections. *Brain* **134**, 2248-2260 (2011). https://doi.org/10.1093/brain/awr161

82 Zhuo, J. *et al.* Diffusion kurtosis as an in vivo imaging marker for reactive astrogliosis in traumatic brain injury. *Neuroimage* **59**, 467-477 (2012). https://doi.org/10.1016/j.neuroimage.2011.07.050

83 Song, S.-K. *et al.* Diffusion tensor imaging detects and differentiates axon and myelin degeneration in mouse optic nerve after retinal ischemia,. *NeuroImage* **20**, 1714-1722 (2003). https://doi.org/10.1016/j.neuroimage.2003.07.005

84 Sun, S. W. *et al.* Differential sensitivity of in vivo and ex vivo diffusion tensor imaging to evolving optic nerve injury in mice with retinal ischemia. *Neuroimage* **32**, 1195-1204 (2006). https://doi.org/10.1016/j.neuroimage.2006.04.212

85 Sahin, S. *et al.* White Matter Evaluation in Multiple Sclerosis Through Magnetic Resonance Kurtosis Imaging. *Cureus* **11**, e6424 (2019). https://doi.org/10.7759/cureus.6424

86 Han, Y., Wu, P., Tian, J., Chen, H. & Yang, C. Diffusion kurtosis imaging and diffusion weighted imaging comparison in diagnosis of early hypoxic-ischemic brain edema. *Eur J Med Res* **28**, 159 (2023). https://doi.org/10.1186/s40001-023-01090-x

87 Veraart, J. *et al.* More accurate estimation of diffusion tensor parameters using diffusion Kurtosis imaging. *Magn Reson Med* **65**, 138-145 (2011). https://doi.org/10.1002/mrm.22603

88 Vanhoutte, G. *et al.* Diffusion kurtosis imaging to detect amyloidosis in an APP/PS1 mouse model for Alzheimer's disease. *Magn Reson Med* **69**, 1115-1121 (2013). https://doi.org/10.1002/mrm.24680

89 Praet, J. *et al.* Diffusion kurtosis imaging allows the early detection and longitudinal follow-up of amyloid-beta-induced pathology. *Alzheimers Res Ther* **10**, 1 (2018). https://doi.org/10.1186/s13195-017-0329-8

90 Richard, K. L., Filali, M., Prefontaine, P. & Rivest, S. Toll-like receptor 2 acts as a natural innate immune receptor to clear amyloid beta 1-42 and delay the cognitive decline in a mouse model of Alzheimer's disease. *J Neurosci* **28**, 5784-5793 (2008). https://doi.org/10.1523/JNEUROSCI.1146-08.2008

91 Ullén, F., Deliagina, T. G., Orlovsky, G. N. & Grillner, S. Visual Pathways for Postural Control and Negative Phototaxis inLamprey. *Journal of Neurophysiology* **78**, 960-976 (1997).

92 Yanez, J., Souto, Y., Pineiro, L., Folgueira, M. & Anadon, R. Gustatory and general visceral centers and their connections in the brain of adult zebrafish: a carbocyanine dye tract-tracing study. *J Comp Neurol* **525**, 333-362 (2017). https://doi.org/10.1002/cne.24068

93 DeKorver, N. W., Chaudoin, T. R. & Bonasera, S. J. Toll-Like Receptor 2 Is a Regulator of Circadian Active and Inactive State Consolidation in C57BL/6 Mice. *Front Aging Neurosci* **9**, 219 (2017). https://doi.org/10.3389/fnagi.2017.00219

94 Moore, H. A. & Whitmore, D. Circadian rhythmicity and light sensitivity of the zebrafish brain. *PLoS One* **9**, e86176 (2014). https://doi.org/10.1371/journal.pone.0086176

5. APPENDIX

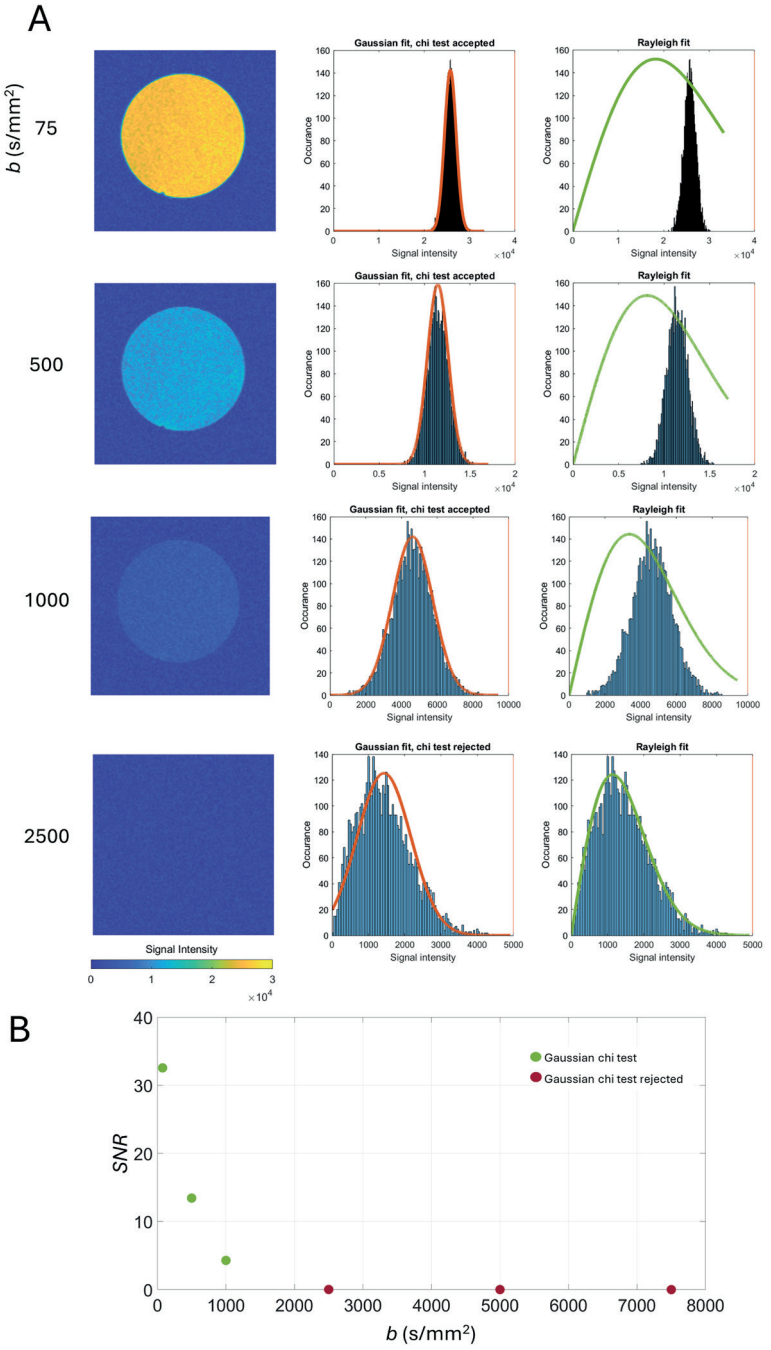
A
b (s/mm²)
75
500
1000
2500
Gaussian fit, chi test accepted
Rayleigh fit
Gaussian fit, chi test rejected
Occurance
Signal intensity
Signal Intensity
B
SNR
b (s/mm²)
Gaussian chi test
Gaussian chi test rejected

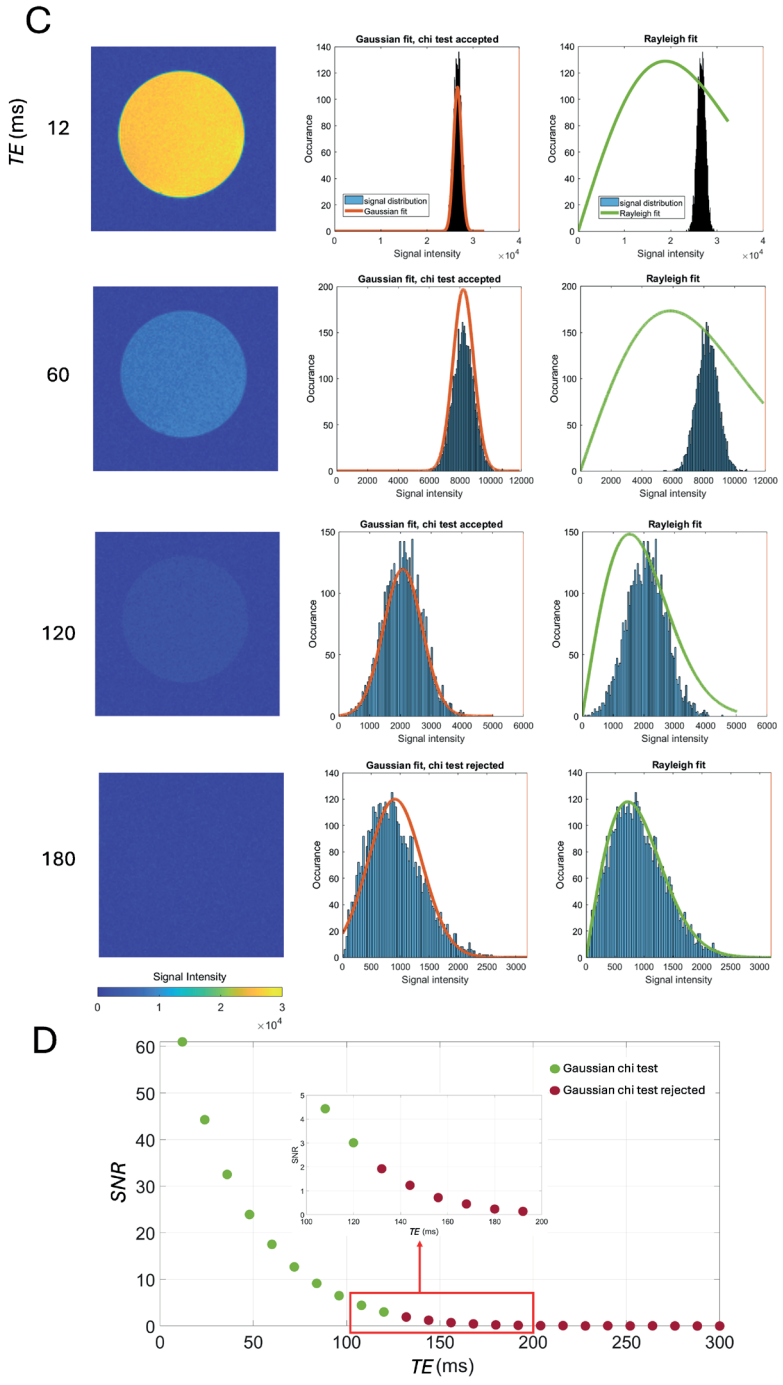
C
TE (ms)
12
60
120
180
Gaussian fit, chi test accepted
Rayleigh fit
Gaussian fit, chi test rejected
Occurance
Signal intensity
signal distribution
Gaussian fit
Rayleigh fit
Signal Intensity
D
SNR
TE (ms)
Gaussian chi test
Gaussian chi test rejected

Figure S3.1. DWI and MSME data profile obtained at 750 MHz, fitted to Gaussian and Rayleigh fit functions. [A] *DWI measurement of $CuSO_4$ in D_2O/H_2O (80%/20%), showcasing the signal intensity profile fitted to a Gaussian and Rayleigh fit.* ***[B]*** *SNR of mean MR signal acquired for $CuSO_4$ in D_2O/H_2O (80%/20%) by DWI at various b-values ranging from 0 to 8000 s/mm^2. According to these the Gaussian chi test performed on the DWI MR signal profile, a Gaussian distribution may be assumed for MR signals with a SNR up to 3.* ***[C]*** *MSME measurement of $CuSO_4$ in D_2O/H_2O (80%/20%), showing the signal intensity profile fitted to a Gaussian and Rayleigh fit at various echo times.* ***[D]*** *SNR of mean MR signal obtained for D_2O/H_2O (80%/20%) by MSME at echo times between 12 and 300 ms. Gaussian chi test of the MR signal profile is accepted the up to an SNR of 3. Acquisition details MSME: TR = 3000 ms, τ = 6.0 ms, ns = 4, resolution 47 × 47 µm, and a slice thickness 500 µm. DWI: TR = 1000 ms, TE = 13 ms, ns = 4, resolution 47 × 47 µm, slice thickness 200 µm, effective b-value range 50, 500, 1000, 1500, 2000, 2500, or 3000 s/mm^2. Figure on the preceding pages.*

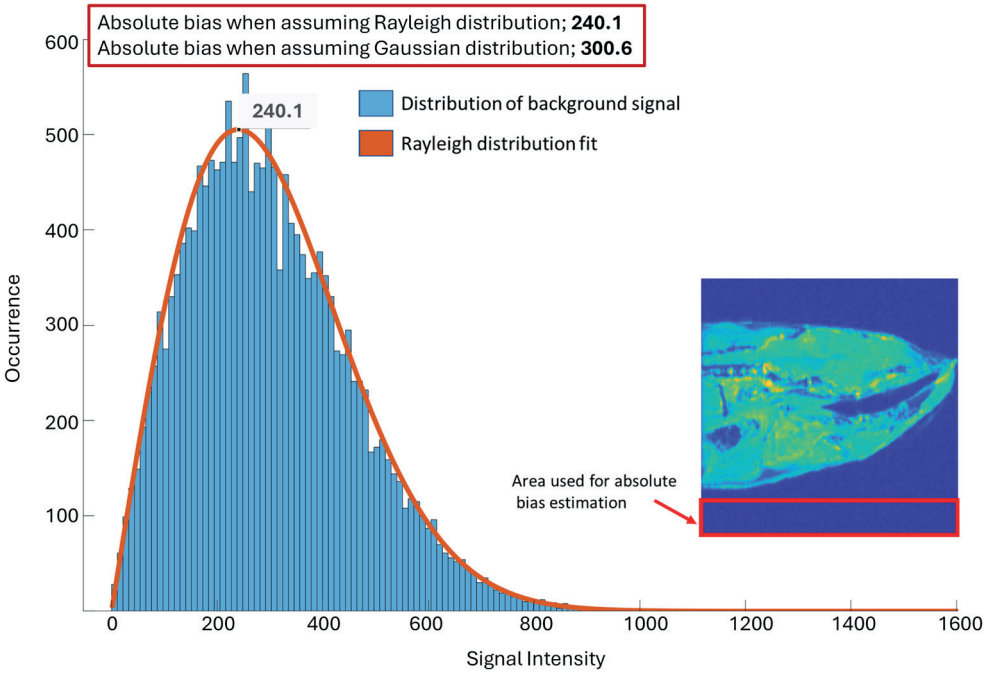

Figure S3.2. Estimation of the absolute bias (systematic error) in DWI at 750 MHz, using Gaussian and Rayleigh fit functions. *[C] Profile of the background signal obtained in a DWI measurement, showing a clear Rayleigh distribution. The plot illustrates how a mean background estimation in the phasor approach by assuming a Gaussian distribution used would overestimates the background signal by 25% compared to the Rayleigh distribution.*

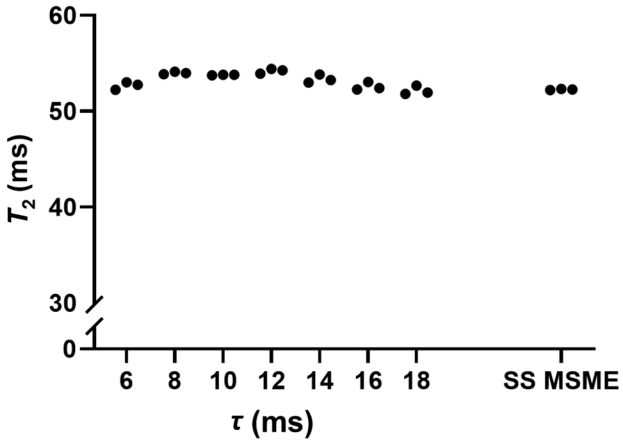

Figure S3.3. Estimated T_2 as a function of CPMG refocusing pulse interval (τ) in multi-slice MSME. *No significant change in the T_2 is observed, indicating reported T_2 are not primarily influenced by magnetic field disturbances. Furthermore, single-slice (SS) MSME was performed for a τ of 6 ms, showing no significant change in T_2 compared to multi-slice MSME, indicating no significant magnetization transfer-related bias of the water signal.*

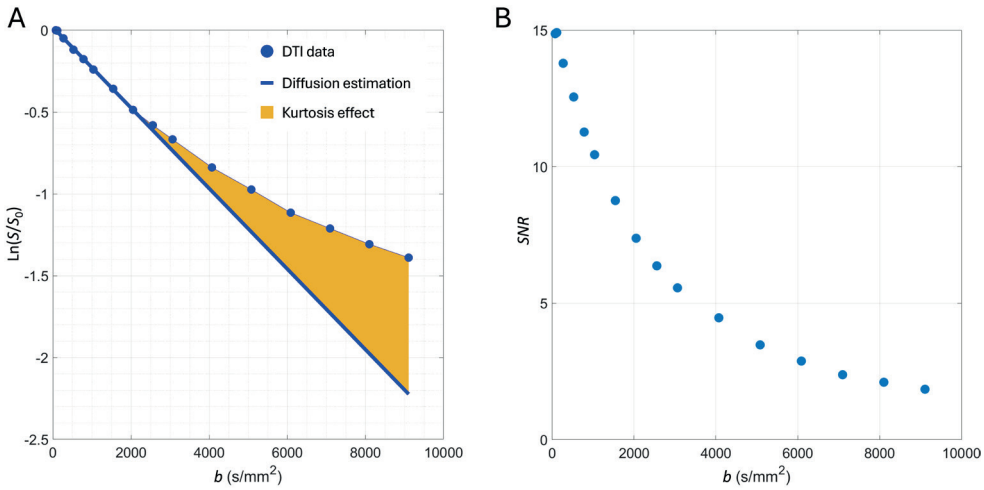

Figure S3.4. Relation between applied b-values in dMRI experiments and the observed kurtosis effect and SNR in the zebrafish brain at 750 MHz. [A] *Relationship between normalized natural logarithmic MR signal obtained by DTI, compared to the expected diffusion-weighted signal and their difference displayed as the kurtosis effect at increasing b-values* ***[B]*** *SNR obtained by DTI at increasing b-values.*

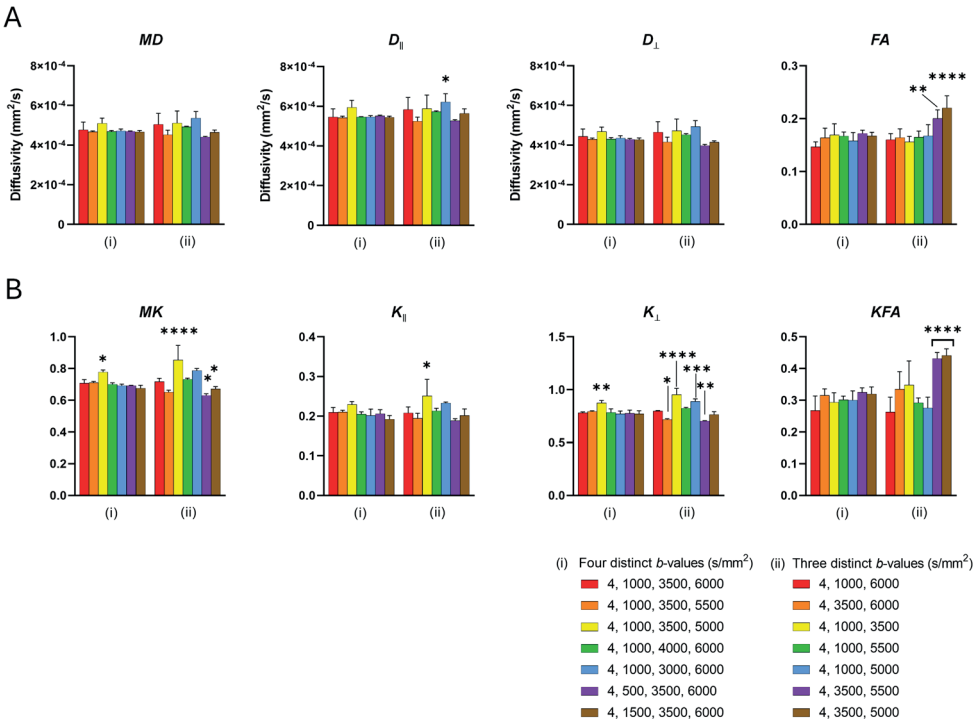

Figure S3.5 Impact of effective b-value range manipulation on diffusion tensor and diffusion kurtosis metrics. *The effect of manipulating the effective b-value range on the estimated* ***[A]*** *diffusion tensor metrics and* ***[B]*** *diffusion kurtosis metrics. (i) The impact of altering the first, second or third b-value shell (b_0 not included) by 500 s/mm² was investigated. The effect on the estimated metrics was found negligible, except if the third b-value shell was lowered to 5000 s/mm², which led to a significant increase in the MK and $K_\perp$ compared to the control. Notably, transitioning from four distinct b-values to three distinct b-values revealed a clear difference, with more statistical variation observed, particularly in the FA and diffusion kurtosis metrics. Data was obtained by conducting repeated DTI measurements (n = 3) on the same zebrafish (control group), extracting data from the cerebellum. Statistical analysis was performed by ordinary one-way ANOVA, comparing the mean of each effective b-value range with the control range applied during measurements, effective b range of 4, 1000, 3500, or 6000 s/mm². A significance level of $p < 0.05$ was employed, denoted by asterisks (*$p < 0.05$, **$p < 0.01$, ***$p < 0.005$, ****$p < 0.001$). Acquisition details: TR = 2000 ms, TE = 12.4 ms, ns = 4, resolution 25 µm × 25 µm × 200 µm, effective b-value range as specified in legend, with 8, 12, 24, or 36 diffusion-encoding directions respectively for the b_0, and the first, second, and third b-value shell.*